JOURNAL OF PETROLOGY | VOLUME 51 | NUMBERS 1 & 2 | PAGES 153–183 | 2010 | doi:10.1093/petrology/egp066

Reaction Processes between Tholeiitic Melt and Residual Peridotite in the Uppermost Mantle: an Experimental Study at 0·8 GPa

GREG VAN DEN BLEEKEN[1]*, OTHMAR MÜNTENER[2] AND PETER ULMER[3]

[1]INSTITUTE OF GEOLOGICAL SCIENCES, UNIVERSITY OF BERN, BALTZERSTRASSE 3, CH-3012 BERNE, SWITZERLAND

[2]INSTITUTE OF MINERALOGY AND GEOCHEMISTRY, UNIVERSITY OF LAUSANNE, ANTHROPOLE, CH-1015 LAUSANNE, SWITZERLAND

[3]INSTITUTE FOR MINERALOGY AND PETROLOGY, ETH ZÜRICH, CLAUSIUSSTRASSE 25, CH-8092 ZÜRICH, SWITZERLAND

RECEIVED DECEMBER 12, 2008; ACCEPTED SEPTEMBER 8, 2009
ADVANCE ACCESS PUBLICATION JANUARY 13, 2010

We present the results of a series of anhydrous piston cylinder experiments that illustrate the mechanisms and implications of reaction between tholeiitic melt and depleted peridotite in the uppermost mantle. To simulate infiltration–reaction processes we have applied a three-layer setup in which a layer of primitive basaltic powder ('melt layer') is consecutively overlain by a 'peridotite layer' and a layer of vitreous carbon spheres ('melt trap'). The peridotite layer is mixed from pure separates of orthopyroxene, clinopyroxene and spinel (Balmuccia peridotite), and San Carlos olivine. Two tholeiitic melt compositions, respectively with compositions in equilibrium with lherzolitic (ol, opx, cpx) and harzburgitic (ol, opx) residues after partial melting at 1·5 GPa, were employed. Melt from the melt layer is forced to move through the peridotite layer into the melt trap. Experiments were conducted at 0·8 GPa with peridotite of variable grain size, in the temperature range 1200–1320°C and for run durations of 10 min to 92 h. In this P–T *range, representing conditions encountered in the transition zone between the thermal boundary layer and the top of the asthenosphere below oceanic spreading centers, the melt is subjected to fractionation and the peridotite is partially melting (T_s ~1260°C). Modal observations indicate a strong dependence between phase relations in the melt layer and changes in the modal abundances of the peridotite layer, as a function of both temperature and melt composition. Textural and compositional evidence, as well as modeling of Fe–Mg profiles in olivine, demonstrates that reaction between percolating melt and peridotite occurs by a combination of dissolution–reprecipitation and solid-state diffusion. Dissolution–reprecipitation leads to well-equilibrated phases whereas diffusional equilibration introduces zoning at experimental timescales. We discuss the observed reaction mechanisms and the consequent compositional changes in the light of local chemical equilibria and reaction kinetics. The results have direct implications for melt migration in upper-mantle thermal boundary layers.*

KEY WORDS: *depleted peridotite; experimental petrology; melt–rock reaction; thermal boundary layer; tholeiitic melt*

INTRODUCTION

There is a continuously growing body of evidence for reaction between upper-mantle partial melts and residual peridotite. A classic example is represented by replacive dunites that are frequently observed in the mantle sections of ophiolites and peridotite massifs (e.g. Boudier & Nicolas, 1972; Quick, 1981; Berger & Vannier, 1984; Kelemen *et al.*, 1995; Suhr *et al.*, 2003). They are interpreted as the result of preferential dissolution of pyroxenes in ascending olivine-saturated primary melts and generally

*Corresponding author. Present address: Institute of Mineralogy and Geochemistry, University of Lausanne, Anthropole, CH-1015 Lausanne, Switzerland. Telephone: +41/(0)21 692 44 40.
E-mail: greg.vandenbleeken@unil.ch

© The Author 2010. Published by Oxford University Press. All rights reserved. For Permissions, please e-mail: journals.permissions@oxfordjournals.org

source: https://doi.org/10.7892/boris.115577 | downloaded: 23.5.2021

assumed to represent the main extraction mechanism for mantle melts (e.g. Kelemen *et al.*, 1997; Stracke *et al.*, 2006). Recently, however, reactive porous flow features have been increasingly recognized in ophiolites and peridotite massifs (e.g. Van der Wal & Bodinier, 1996; Rampone *et al.*, 1997; Takahashi, 2001; Dijkstra *et al.*, 2003; Müntener *et al.*, 2005; Zhang, 2005; Le Roux *et al.*, 2007), and in mantle rocks sampled at magma-poor slow-spreading oceanic ridges and transform faults (e.g. Elthon, 1992; Seyler & Bonatti, 1997; Seyler *et al.*, 2004). Moreover, regional-scale modification of ancient subcontinental mantle by melt infiltration and melt–rock reaction during incipient opening of oceanic basins in ocean–continent transition zones has been recognized (Müntener & Piccardo, 2003; Müntener *et al.*, 2004). The evidence for melt–rock interactions in the mantle is thus extensive, encompassing textural relations and mineral modes, major to minor element phase compositions, melt inclusions (e.g. Sobolev & Shimizu, 1993; Schiano *et al.*, 1994; Kamenetsky & Crawford, 1998; Kamenetsky *et al.*, 2001), isotope systematics, and local to regional variations in mid-ocean ridge basalt (MORB) chemistry (e.g. Langmuir *et al.*, 1992; le Roux *et al.*, 2002). Nonetheless, numerous questions regarding the controls on precise reaction processes between ascending partial melts and peridotite, and the consequent modes of melt transport remain to be addressed adequately. This is particularly the case for the transitional region or 'thermal boundary layer' (see White, 1988) of the uppermost mantle, where the local geotherm deviates from the adiabatic (mantle) geotherm but conductive heat-loss to the surface does not yet dominate over advection of heat from below (as is the case for the lithosphere).

Direct observation of upper-mantle processes is impractical. Both the reacted mantle rocks and melts will undergo significant alteration and modification on their way from upper-mantle depths to the surface. It is, therefore, crucial to perform experimental investigations to attain better understanding of the first-order reaction processes. A number of experimental studies broadly related to upper-mantle melt–rock reaction processes have been carried out to date (Kelemen *et al.*, 1990; Daines & Kohlstedt, 1994; Lundstrom, 2000, 2003; Morgan & Liang, 2003, 2005; Beck *et al.*, 2006). Furthermore, there is a larger body of studies dealing with the systematics of and processes related to partial melting in the upper mantle (e.g. Draper & Green, 1999; Hirschmann, 2000; Pickering-Witter & Johnston, 2000; Lo Cascio *et al.*, 2004; Schiano *et al.*, 2006; Falloon *et al.*, 2008; and references therein). These experimental studies, combined with a number of numerical studies dealing with melt–rock reaction and reactive melt flow (e.g. Ortoleva *et al.*, 1987; Aharonov *et al.*, 1995; Asimow & Stolper, 1999; Wark & Watson, 2000; Spiegelman *et al.*, 2001; Liang, 2003; Liang & Guo, 2003), have contributed significantly to the understanding of melt–rock reaction. One general outcome of these studies is the recognition of the complexity of upper-mantle partial melting and melt–rock reaction processes, which are mutually dependent on a number of intensive (e.g. P–T, fO_2 conditions, thermochemical phase and liquid properties) and non-intensive parameters (e.g. grain size, interconnected porosity, and other textural relationships).

To our knowledge, melt-infiltration experiments have not yet been performed with primitive upper-mantle partial melts at the P–T conditions encountered in thermal boundary layers (TBLs) within the upper mantle. The experimental reaction studies by Daines & Kohlstedt (1994) and Morgan & Liang (2003, 2005) were designed to investigate melt–peridotite reaction and formation of reactive boundary layers (RBLs), with applications to melt flow regimes in the upper mantle. However, fine-grained ($\leq$10 μm) peridotite analogues were employed, resulting in important kinetic effects on grain-scale reaction processes that were not considered (as will be shown below). Furthermore, the melt compositions used by Morgan & Liang are more reactive than typical partial melts expected to percolate through the TBL in adiabatically upwelling domains of the upper mantle. Additionally, the experiments reported by Daines & Kohlstedt (1994) were performed at fairly low, probably unrealistic pressures of 0·3 GPa. Consequently, these studies are not directly applicable to reactive melt flow (organization) in TBLs within the upper mantle, especially as upper-mantle partial melts entering the TBL will be subject to an entire range of interrelated processes, such as fractional crystallization, diffusive equilibration through the melt and the solid phases, and dissolution ± reprecipitation of phases.

This contribution presents the results of a comprehensive experimental study with applications to reactive melt transport in upper-mantle TBLs below slow- to ultraslow-spreading mid-ocean ridges. Our experiments serve to examine melt–rock interactions that potentially occur in ocean–continent transition zones and beneath oceanic spreading centers. The general objective of this experimental study is to derive a consistent set of data to evaluate the compositional and time-dependent evolution of migrating magma over a range of temperatures and pressures as a function of initial melt and peridotite composition. The ultimate goal is to provide a tool to understand infiltration and crystallization mechanisms operating in natural peridotites within the thermal boundary layer under oceanic spreading centers. This information might, in turn, be used to interpret microstructures in infiltrated peridotites; the chemical compositions of natural peridotite constituents could be utilized in future to provide better estimates of the compositions of the infiltrating magmas. Here we focus on the different reaction processes

proceeding during melt–peridotite equilibration by thorough evaluation of textural and modal changes during melt–peridotite reaction and the consequential changes in mineral compositions. The related compositional evolution of the infiltrating liquid will be discussed in detail in a separate paper.

EXPERIMENTAL METHODS

Melt–peridotite reaction processes were studied in a series of experiments in which a layer of primitive basaltic powder is consecutively overlain by a peridotite layer and a layer of vitreous carbon spheres (Fig. 1). The porosity of the melt trap should enhance flow of melt into the peridotite layer, thereby promoting reactive melt percolation. In addition, the melt trap conserves the reacted melts for chemical analysis. The three-layered experimental charge is contained in a graphite container that tightly fits in a Pt capsule (Fig. 1). Experiments were carried out at P–T conditions appropriate for those in the thermal boundary layer underneath oceanic spreading centers (i.e. 1200–1290°C and 0·8 GPa). The starting materials employed in this study are listed in Table 1.

Starting materials

As a melt analogue, we initially used the primitive basaltic glass composition HK#19.1 (Villiger *et al.*, 2004) that is in equilibrium with a lherzolitic residue (ol, opx, cpx) at 1·5 GPa and 1350°C (Hirose & Kushiro, 1993). Villiger and coworkers performed a comprehensive set of fractional and equilibrium crystallization experiments on this composition at P and T conditions relevant for our study (Villiger *et al.*, 2004, 2007). This microscopically heterogeneous starting material proved to be prone to disequilibrium melting during the initial stages of heating, producing 'exotic melts' as they will be referred to hereafter. Therefore, we vitrified HK#19.1 under controlled fO_2 in a gas-mixing furnace, producing the starting composition 'HK19.v'. The vitrification process (decreased FeO content), followed by grinding to a fine-grained powder of the resultant glass in an agate mortar (increased SiO_2 content) introduced small compositional changes to the starting composition (see Table 1). A second melt analogue was subsequently mixed (and vitrified) to test the influence of melt composition on melt–rock reaction. This second analogue is in equilibrium with a harzburgitic residue (ol, opx) at 1·5 GPa and 1400°C corresponding to the melt phase in run 20 of Hirose & Kushiro (1993) and was

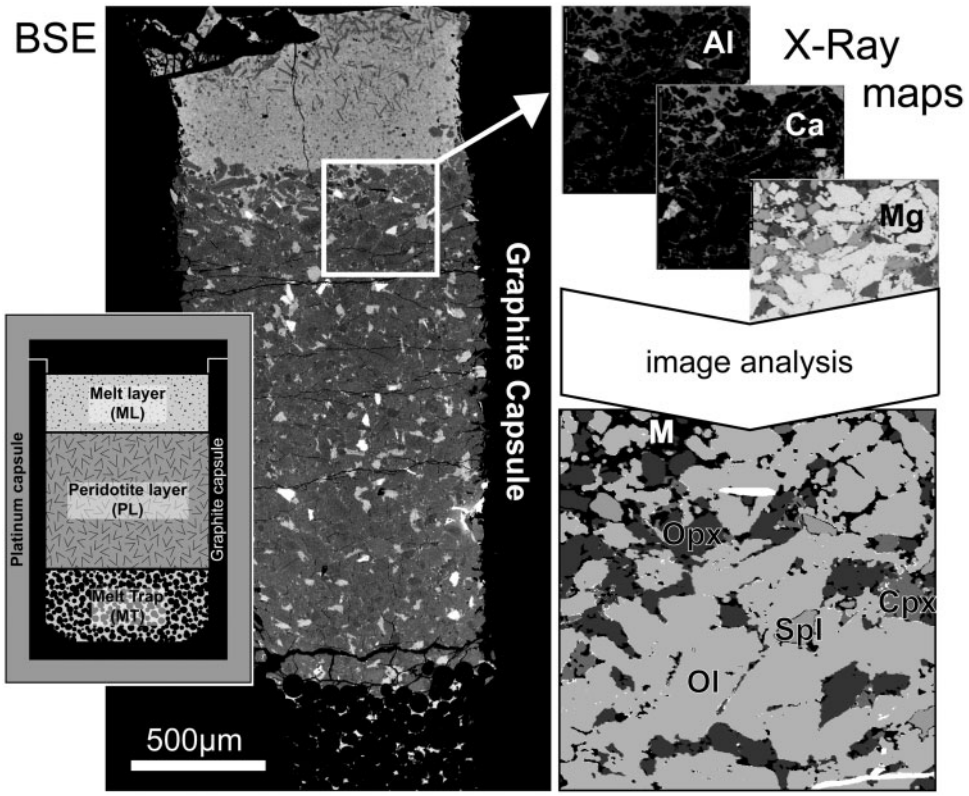

Fig. 1. Schematic illustration of the three-layer experimental setup contained in a double Pt–C capsule used in this study (inset on the left-hand side) and BSE image of a recovered experimental charge. Examples of X-ray maps of the highlighted area are shown on the right, together with the resulting map after image analysis.

Table 1: Electron microprobe analyses of starting materials and calculated BaSC starting mix compositions

	HK#			Balmuccia						San Carlos		BaSC	
	19.1	19.v	20.v	Opx ($n=8$)		Cpx ($n=14$)		Sp ($n=10$)		Ol ($n=13$)		1 & 3	2
				Av	SD	Av	SD	Av	SD	Av	SD		
SiO_2	49·07	50·17	50·29	56·16	0·60	52·92	0·35	0·01	0·01	41·02	0·14	44·91	45·14
TiO_2	0·60	0·60	0·40	0·07	0·01	0·26	0·03	0·14	0·03	0·00	0·01	0·05	0·05
Cr_2O_3	0·36	0·35	0·20	0·49	0·17	1·04	0·15	24·60	1·60	0·02	0·01	0·70	0·72
Al_2O_3	15·28	15·26	14·18	3·23	0·67	4·29	0·40	42·69	1·71	0·02	0·01	2·00	2·07
FeO_{tot}	7·50	6·62	6·93	5·97	0·23	2·15	0·21	17·16	0·63	8·87	0·66	7·75	7·65
MnO	0·14	0·17	0·15	0·15	0·02	0·07	0·02	—	—	0·13	0·02	0·13	0·13
NiO	—	—	—	0·07	0·02	0·04	0·02	0·16	0·02	0·36	0·02	0·26	0·25
MgO	13·04	12·66	15·85	33·38	0·47	15·58	0·65	15·54	0·56	49·19	0·62	41·77	41·29
CaO	12·31	12·45	10·99	0·38	0·09	22·49	0·71	0·00	0·00	0·07	0·01	2·12	2·37
Na_2O	1·57	1·56	0·94	0·03	0·02	0·96	0·06	0·00	0·01	0·00	0·01	0·09	0·10
K_2O	0·08	0·09	0·04	0·00	0·00	0·00	0·00	0·00	0·00	0·00	0·00	0·00	0·00
Total	100·00	100·00	100·00	99·95	0·42	99·79	0·51	100·30	0·48	99·70	0·34	99·78	99·78
Mg-no.	0·76	0·77	0·80	0·91	0·00	0·93	0·01	0·62	0·02	0·91	0·01	0·91	0·91
Cr-no.								0·28	0·02				

BaSC compositions were calculated by proportionally summing ol, opx, cpx and sp compositions as determined by EMP. Dashes indicate that the element was below the detection limit. Av, average; SD, standard deviation; *n*, number of analyses.

accordingly named HK#20.v. To improve readability, we use the acronyms 'HK#19' and 'HK#20' hereafter, unless we specifically want to distinguish between 'HK#19.1' and 'HK#19.v'. As a result of a higher Ca/Si ratio in HK#19 compared with HK#20, cpx fractionation is favored in HK#19 whereas opx fractionation is favored in HK#20.

The peridotite analogues consist of recombined powders obtained from hand-picked separates of natural grains. Although the use of natural grains has been debated for melting studies (e.g. Falloon *et al.*, 1999), we opted to use natural grains in this melt–rock reaction study. Our goal was not to reach complete equilibration for all grains, but to perform experiments that allow the study of melt–rock reactions as they could occur in the upper mantle. Low-Ca orthopyroxene, high-Ca clinopyroxene and Cr-spinel were separated from the Balmuccia peridotite (Ivrea–Verbano Zone, Northern Italy), whereas the olivine used originates from the San Carlos Volcanic Field (Arizona). Final equilibration of the Balmuccia spinel lherzolite took place at 850–950°C and ~1·0 GPa (Shervais, 1979). San Carlos spinel lherzolite xenoliths gave two-pyroxene equilibration temperatures of 1050°C (Brey & Köhler, 1990) and a pressure of 1·3 GPa (Köhler & Brey, 1990). Average compositions of the minerals and calculated starting mix compositions are listed in Table 1. The mineral separates were ground separately under ethanol and sieved to obtain well-defined grain-size fractions. From these separates two starting fractions were mixed: BaSC1 (200–80 μm) and BaSC2 (80–30 μm), with 'BaSC' indicating derived from 'Balmuccia–San Carlos'. BaSC1 has a composition (in wt %) of 65 ol, 24 opx, 9 cpx, 2 spl, whereas BaSC2 contains 63 ol, 25 opx, 10 cpx, 2 spl. Both compositions represent depleted lherzolite, with a solidus temperature of ~1260°C (inferred from forward melting of BaSC2 at 1260°C and 0·8 GPa, displaying incipient melting). A third starting material, BaSC3, was produced by grinding BaSC1 under ethanol for 30 min. This resulted in a 'porphyritic' mix of larger grains (up to 50 μm) embedded in a fine-grained groundmass (<10 μm).

All starting materials were dried at 220°C for at least 24 h to drive off any adsorbed water and subsequently stored in an oven at 110°C. For the more hygroscopic melt analogues, heat-treatment at 220°C was always repeated prior to loading of the capsules. Starting materials were taken out of the oven just before loading of a capsule.

Experimental set-up

To minimize Fe loss to the noble metal capsule and to constrain fO_2 near the C–CO_2–CO equilibrium, a Pt–graphite double-capsule technique was applied (Ulmer & Luth, 1991). Layers of vitreous carbon, peridotite and

basaltic powder were sequentially loaded into a graphite container [3·4 mm outer diameter (o.d.), 2 mm inner diameter (i.d.)] that was closed with a tight-fitting lid. The graphite container was placed in a Pt capsule (4 mm o.d.) that was welded shut only after additional drying for several hours at 110°C. The Pt capsules were checked for leakage by weighing prior to and after submersion in acetone.

All experiments were conducted in a 14 mm bore end-loaded Boyd & England (1960) type solid-media piston cylinder apparatus at the high-pressure laboratory at ETH Zürich. Initially, salt–Pyrex–MgO, and later talc–Pyrex–MgO assemblies were employed, with a friction correction of ~3% and ~10% respectively applied to the nominal pressure. Temperature was measured with $Pt_{94}Rh_{06}$–$Pt_{70}Rh_{30}$ (B-type) thermocouples with an estimated accuracy of ±10°C, without accounting for pressure effects on the e.m.f. Temperature increments of 30°C were used for successive experiments, considering temperature reproducibility of ±15°C in piston cylinder experiments.

Runs were gently cold pressurized to 0·4 GPa, before temperature was raised at a rate of 80°C/min. From ~700°C the pressure was gradually increased along with the temperature until annealing conditions were attained. To ensure that no melt migration and subsequent reaction took place, annealing had to be performed in the subsolidus domain. In earlier experiments (up to GB17) we annealed runs using the HK#19.1 composition at 1100°C, resulting in percolation of a small fraction of exotic melt into the peridotite layer (PL) and melt trap (MT). Later experiments were annealed at 1000°C to prevent migration of the melt at this stage. After 5 h of annealing, the temperature was increased to the desired values at rates between 150 and 200°C/min. Experiments were quenched by shutting off the power supply, resulting in quenching rates of the order of 200–300°C/s for the first 600°C. After the experiment, the recovered charge was sectioned longitudinally, mounted in epoxy and polished for microanalysis. Most experiments were kept at run temperature for 15 h, but several shorter and a few longer runs were performed to bracket the results of the 15 h runs. Here, we focus on the results of the 15 h runs.

Microprobe analysis

Wavelength-dispersive analyses as well as backscattered electron (BSE) images and X-ray concentration maps were acquired on a JEOL JXA-8200 Superprobe at the Geological Institute of the University of Bern (Switzerland). An accelerating voltage of 15 kV was applied for all analyses. Crystalline phases were measured with a beam current of 20 nA and a focused beam, whereas quenched liquids were analyzed with 7 nA beam current and 1–10 μm beam size, depending on the sizes of the melt pools. Well-characterized minerals and synthetic compounds were used as standards and the PRZ (CITZAF) correction procedure was applied to the raw data. Peak position counting times were 20 s for all elements, except for Na, which was counted for only 6 s to avoid Na migration, and Ni, which was counted for 30 s. Averaged measurements ($n = 10$) of the homogeneous glass SV75 (from Villiger *et al.*, 2007) did not reveal any dependence of element concentrations as a function of spot size (i.e. 1, 5 or 10 μm). The detection limit for the various elements was typically between 0·01 and 0·03 wt %, except for NiO with a detection limit of ~0·12 wt %. Structural formulae of olivine and spinel, pyroxene and plagioclase were calculated on the basis of 4, 6 and 8 oxygen atoms, respectively.

Image analyses

Modal proportions of the various mineral phases and melt were quantified using a combination of automated and non-automated image analysis. To allow for good distinction between the various mineral phases and melt, X-ray concentration maps for Ca, Mg and Al were made on the electron microprobe (EMP). Three 400 μm × 400 μm maps were obtained for every charge: one of the melt layer (ML), one of the PL adjacent to the ML, and one starting ±500 μm from the ML–PL interface. Distinction between the various solid phases and melt was easily possible by utilizing combinations of Mg, Al and Ca maps and employing the software package ImageJ. We have adopted the work-flow described by Lydon (2005) to our study.

RESULTS

In total, 41 experiments were conducted at 0·8 GPa; of these, one was a simple melting experiment of BaSC2 at 1260°C and three reaction experiments were terminated directly after 5 h of annealing (hereafter referred to as HIP-only runs). The HIP-only runs served to determine the conditions for annealing so that no liquid from the ML would be lost to the PL during the annealing stage. All other experiments represent reaction experiments run between 1200°C and 1320°C; not all of them were entirely successful. Physical mixing of the different layers occasionally occurred in the earliest experiments, most probably as a result of insufficient packing of the graphite container with the starting materials. Once that problem was overcome, the three-layer geometry remained intact during almost all successive experiments (e.g. Fig 1). In some runs one or a few grains drifted from the PL into the ML, but this should not have had a significant effect on the ML composition. An additional problem encountered occasionally was inaccuracy of the applied temperature. As noted above, temperature reproducibility in piston cylinder experiments is typically estimated to be ±15°C. However, as a result of thermocouple contamination the actual run temperature can differ significantly from the prescribed value, as described by Yaxley (2000).

Table 2: Experimental run conditions and phase assemblages of selected runs

Run no.	Per. mix	*T* (°C)	*t* (h)		Run products	RBL
Runs with liquid composition HK#19.1						
GB08	BaSC2	1290	15	ML	liq, ol, sp, cpx***	
				PL	liq, ol, sp**, opx*, cpx***	Dn
GB06	BaSC2	1230	15	ML	liq, ol, sp, cpx	
				PL	liq, ol**, sp**, opx**, cpx**	—
GB14	BaSC2	1200	15	ML	liq, ol, cpx, opx, plg	
				PL	liq, ol**, sp**, opx**, cpx**	—
GB16	BaSC2	1200	91	ML	liq, ol, cpx, opx, plg	
				PL	liq, ol**, sp**, opx**, cpx**	—
GB23	BaSC3	1290	15	ML	liq, ol, sp, cpx***	
				PL	liq, ol, sp**, opx*, cpx***	Dn
GB24	BaSC3	1260	15	ML	liq, ol, sp, cpx	
				PL	liq, ol**, sp**, opx**, cpx**	Dn
GB20	BaSC3	1230	15	ML	liq, ol, sp, cpx, opx	
				PL	liq, ol**, sp**, opx**, cpx**	Wh
Runs with liquid composition HK#19.v						
GB40	BaSC2	1260	15	ML	liq, ol	
				PL	liq, ol**, sp*, opx**, cpx**	—
GB41	BaSC2	1230	15	ML	liq, ol, cpx, plg	
				PL	liq, ol**, sp*, opx**, cpx**	—
Runs with liquid composition HK#20.v						
GB37	BaSC2	1290	15	ML	liq, ol, sp, opx?	
				PL	liq, ol, opx**	—
GB33	BaSC2	1240	15	ML	liq, ol, opx, cpx	
				PL	liq, ol**, sp**, opx**, cpx**	—
GB34	BaSC2	1250	15	ML	liq, ol, opx, cpx***	
				PL	liq, ol**, sp**, opx**, cpx**	Hz
GB35	BaSC2	1200	15	ML	liq?, ol, opx, cpx, plg	
				PL	liq/plg, ol**, sp*, opx**, cpx**, plg	—

*Remnant cores, often with diffusive equilibration towards rims; **newly (re-)precipitated + remnant cores; ***quench. ML, melt layer; PL, peridotite layer; RBL, reactive boundary layer; Wh, wehrlite; Hz, harzburgite; Dn, dunite.

This occurred in some of our runs, but through careful comparison of all experimental phase assemblages and compositions, 'true' run temperatures for these runs could be estimated.

Run conditions and phase assemblages for selected runs are given in Table 2. A general textural overview of the PLs as a function of temperature is provided in Fig. 2; Fig. 3 displays the modal variations of selected runs.

Textural and modal observations

Melt layers (MLs)

Phases precipitated in the ML are euhedral to subhedral at temperatures of 1230°C and above, but often anhedral at 1200°C. Quench crystallization occurred in experiments using HK#20 at temperatures of 1230°C and 1260°C and is represented by large amounts of up to 5 μm long feathery cpx crystals that commonly nucleated on opx and larger (stable) cpx. In the 1200°C HK#20 experiment (GB35) some quench crystallization might also be present, but this is difficult to recognize because of the small grain size and extensive crystallization. All ML phases appear unzoned in BSE images, except for some occasional cpx.

The modal abundances of the melt layers change considerably over the investigated temperature interval and are different for the two melt analogues HK#19 and HK#20 (Fig. 3a). Determination of ML modal compositions is complicated in the case of quench crystallization. Hence ML pyroxene modes for experiments involving

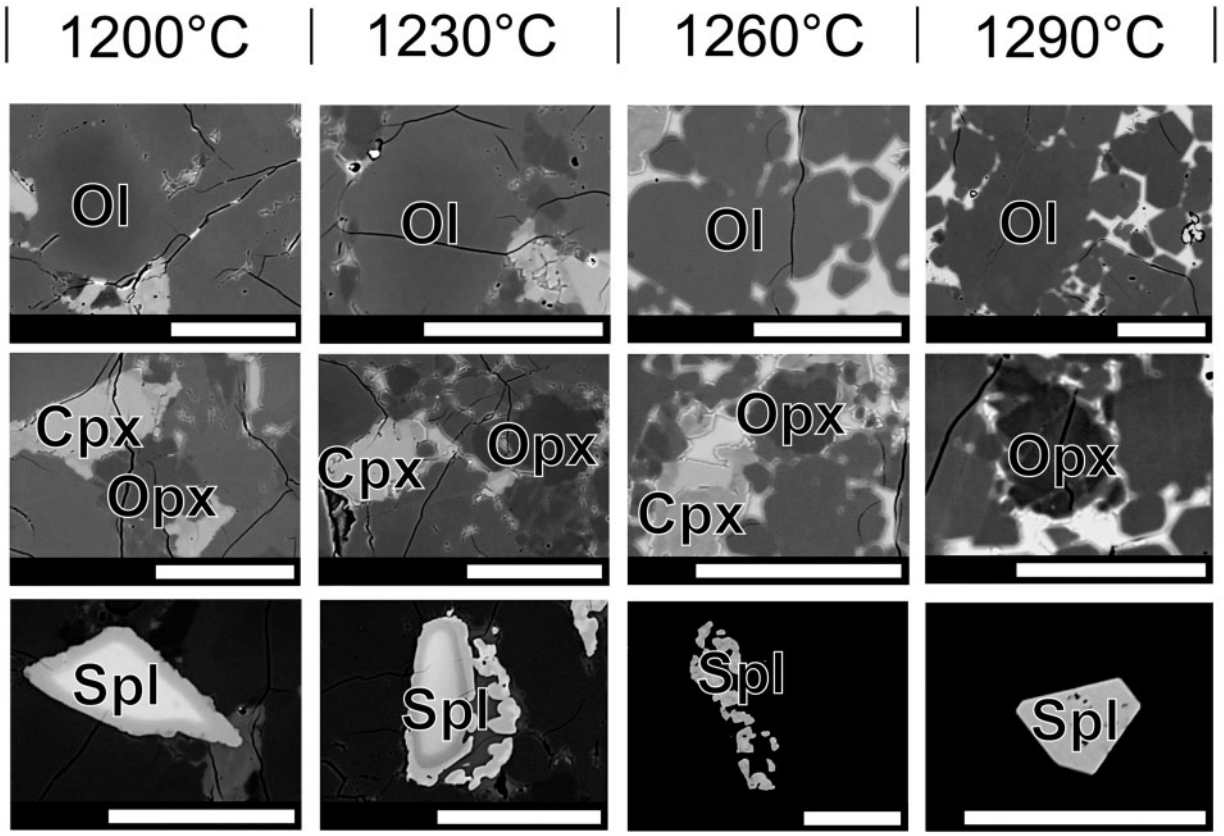

Fig. 2. Representative BSE images illustrating the textural evolution of PLs as a function of run temperature. The initial starting mix texture of irregular angular grains stays recognizable throughout the temperature range, but is progressively obscured towards higher temperature as a result of a combined effect of diffusion and dissolution ± reprecipitation. Olivine and spinel show continuous (diffusive) zoning at 1200 and 1230°C. Spinel, cpx and opx clearly undergo partial dissolution with or without reprecipitation of subhedral or euhedral overgrowths and melt pocket precipitates. Melt pockets become larger and the melt fraction increases with increasing run temperature. The length of the scale bar represents 50 μm in the respective images.

HK#20 are subject to considerable uncertainties below 1290°C. They are probably overestimated at the expense of melt for experiments GB33, GB34 and GB35, probably to varying degrees. Moreover, phases formed in MLs from 1200°C experiments are too fine-grained to allow accurate image analysis. Nonetheless, some systematic modal variations as a function of temperature and starting composition can be observed in Fig. 3a. Olivine occurs throughout the investigated temperature range, with modes increasing with temperature from ~5% at 1230°C to ~32% at 1290°C for HK#19, and from ~3% at 1200°C to ~11% at 1290°C for HK#20. Cpx occurs for both starting compositions at temperatures below 1260°C. When excluding quench cpx (i.e. cpx smaller than ~5 μm; see Fig. 3 caption), modal abundances of cpx as a function of temperature are higher for HK#19 than for HK#20. Opx precipitated from HK#19.1 only at 1200°C, whereas for HK#20 it persists to temperatures of 1250°C. Plagioclase occurs in all runs at 1200°C for both HK#19.1 and HK#20 in the MLs. Using the vitrified equivalent HK#19.v, at 1230°C (GB41) ~8% plagioclase crystallized as 60 μm long prismatic crystals. Spinel was formed only in HK#19.1 (~2% at 1230°C and ~0·2% at 1290°C) and not in the vitrified equivalent or in HK#20. The differences in spinel and plagioclase stability between HK#19.1 and HK#19.v runs reflect a small compositional difference (see Table 1). For HK#19, estimated melt proportions decrease with increasing temperature from ~78·5% at 1230°C to ~68% at 1290°C. For HK#20, the trend as a function of temperature is less consistent, but melt fractions appear to be higher than for equivalent HK#19 runs (e.g. at 1290°C ~89% vs ~68% for HK#20 and HK#19.1, respectively). Phase stability as a function of temperature in MLs of runs with HK#19.1 correlates perfectly with the 0·7 GPa crystallization experiments of Villiger *et al.* (2007). However, as a result of interactions with the PL, modal abundances of the stable phases at any given temperature can differ significantly.

Peridotite layers (PLs)

The textures of grains in the PL after the HIP stage still correspond to those of the BaSC starting mixes.

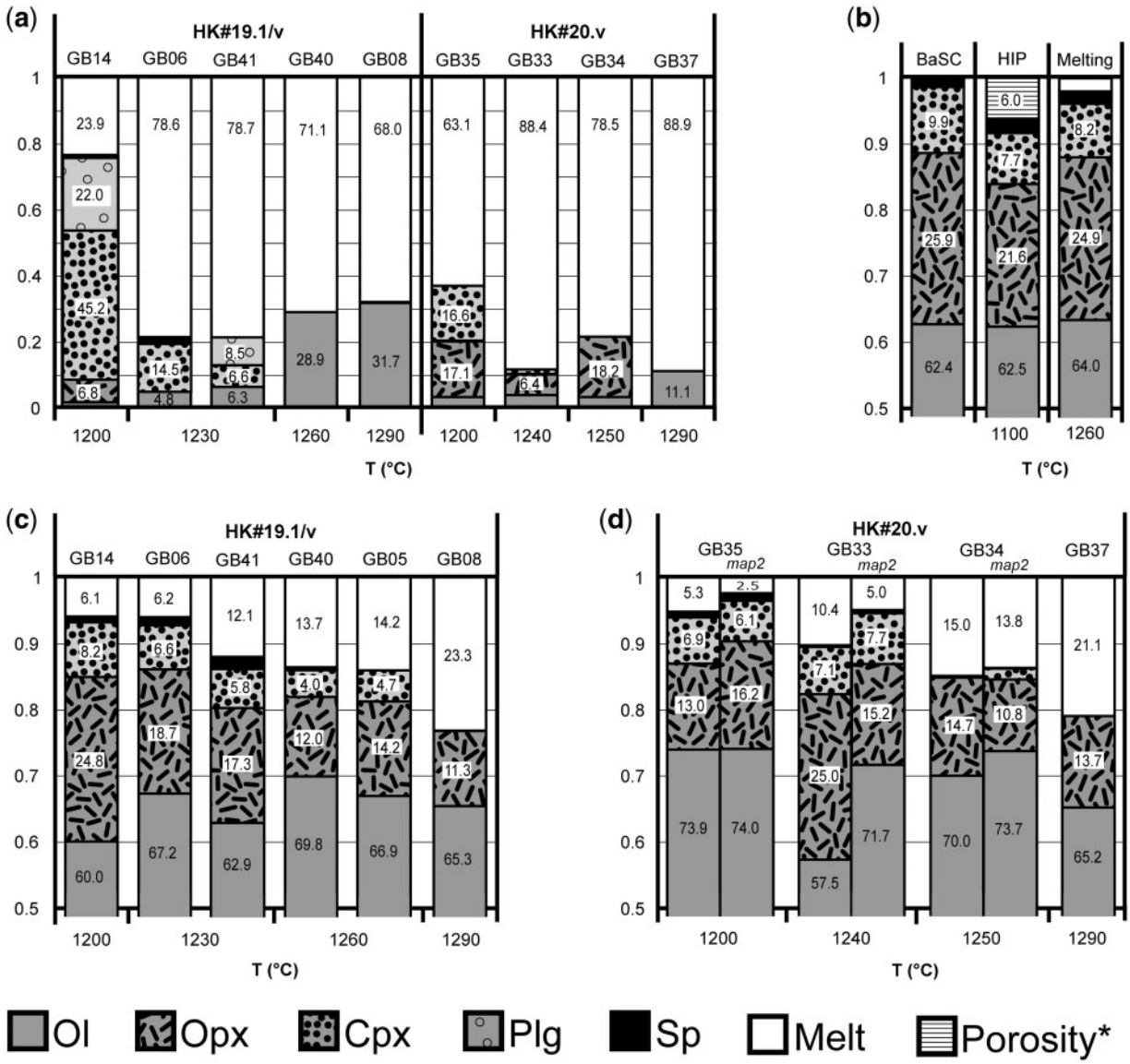

Fig. 3. Bar diagrams displaying melt and solid fractions for selected runs as a function of temperature. (a) Modal compositions of melt layers for HK#19.1/v and HK#20.v, respectively. Up to 10 area % of quench-cpx was formed in runs GB33 and GB34 (recognizable by the feathery shape and sizes <10 μm), which was subtracted from cpx and added to the liquid volume. (b–d) compare PL modal compositions. (b) The BaSC starting composition is compared with a HIP-only run at 1100°C and a simple melting experiment performed at 1260°C. (*'Porosity' in the HIP-only run was determined by quantification of the melt fraction, as this represented unreacted infiltrated ML liquid; see discussion.) (c, d) Modal compositions of BaSC coupled with HK#19.1/v and HK#20.v, respectively. (d) Map2 modes are those of maps that are situated between 500 and 1000 μm from the ML–PL interface. All other modes listed in (c) and (d) are 400 μm × 400 μm areas adjacent to the ML–PL interface, as most reaction occurs in this area. (For detailed discussion of the modal compositions displayed here, see text.)

After partial annealing, grains are somewhat irregularly shaped and unzoned, and ~6% of porosity remains, as observed in HIP-only experiments. Figure 2 illustrates that this initial texture remains recognizable for run temperatures up to 1290°C, but it is increasingly obscured at higher temperature. The PL becomes texturally more equilibrated with increasing temperature and the volume of melt pockets increases. The grain-scale textures displayed in Fig. 2 reveal the different melt–peridotite reaction processes responsible for this textural evolution. At 1200 and 1230°C, olivine has continuous core-to-rim zoning, which is indicative of diffusive equilibration. At 1200°C this results in asymmetric zoning in grains that are in direct contact with the ML, with a wider and more pronounced diffusion zone on the side facing the interface (see also Fig. 5a). Original Balmuccia opx and cpx grains exhibit dissolution features at all temperatures, with or without reprecipitation along initial grains and in adjacent

Table 3: Influence of starting peridotite heterogeneity on image analysis results

	Partial 1	Partial 2	Partial 3	Partial 4	Partial 5	Partial 6	Total area	SD
Ol	65·1	68·1	68·4	67·7	65·1	68·7	67·2	1·6
Opx	18·3	16·9	20·7	20·7	19·0	17·3	18·7	1·7
Cpx	5·4	5·6	6·6	6·2	9·1	7·1	6·6	1·3
Sp	2·1	1·6	0·6	0·7	1·5	1·0	1·2	0·6
Melt	9·0	7·7	4·6	4·6	5·4	5·9	6·2	1·8

Comparison between modal abundances of six partial areas and that of the total area, as determined by image analysis (see text for a detailed discussion). SD, standard deviation.

melt pockets. For example, Fig. 2 illustrates reprecipitation for the selected cpx grains at 1260°C; a small remnant core is lined by darker precipitates with a sharp divide between them. Although not visible in Fig. 2, rims of newly grown opx of a few micrometers thickness occur on old cores in HK#19 experiments (e.g. GB40, GB41) and 10–50 μm thick rims plus euhedral precipitates in melt pockets occur in equivalent HK#20 experiments (e.g. GB33, GB34). Small euhedral to subhedral ol and cpx grains that line melt pockets, or that are formed within them, are also probably the result of dissolution–reprecipitation. The spinel grain at 1200°C in Fig. 2 shows continuous zoning towards a dark rim, whereas at 1230°C spinel is surrounded by additional lighter-colored spongy precipitates resulting from dissolution–reprecipitation. Small anhedral plagioclase was observed only in the PL of run GB07, which is one out of three 1200°C runs employing HK#19.1; this plagioclase-bearing zone extends ~200 μm into the peridotite layer.

Textural observations on the scale of the experimental charge reveal that reaction features often appear most intense near the ML–PL interface. This commonly leads to an increase of the melt-filled porosity and sometimes to a reactive boundary layer (RBL) adjacent to and parallel to the ML–PL interface. For example, in run GB34 the development of a cpx-free RBL, ~380 μm in width, in the PL adjacent to the ML, and in GB08 an ~100 μm wide opx-free RBL, can be observed. The formation of RBLs will be discussed further below.

Quantification of PL modal abundances by image analysis provides further information on reaction processes and progress. Quench crystallization is subordinate and does not significantly influence the calculated mineral modes. However, calculated PL modes are possibly subject to uncertainties as a result of initial BaSC heterogeneity and heterogeneous melt distribution. This was investigated by mapping an area of experiment GB06 six times larger than the normal 400 μm × 400 μm mapping areas. Image analysis was performed on this enlarged area, and, additionally, it was divided into six equal partitions perpendicular to the ML–PL interface. Mineral modes calculated for these areas are listed in Table 3, together with the modal composition of the total (integrated) area. Results reveal some heterogeneous distribution of phases and melt pockets and provide a quantitative estimate for the resulting uncertainty in the determinations of the modal abundances.

Figure 3b compares the theoretical PL mode of BaSC with a simple melting experiment run at 1260°C and a 1100°C HIP-only experiment where melt migrated into the PL without inducing visible reaction. The latter illustrates that the HIP stage does not alter the PL modal composition, and that ~6% porosity remains. At the solidus of our peridotite mix, we envisage a temperature of ~1260°C at 0·8 GPa. The most applicable formula to calculate the solidus of BaSC is the formula of Wasylenki *et al.* (2003), determined on the compositionally similar DMM1. This resulted in a theoretical solidus of 1286·3°C at 1·0 GPa. According to the formula of Hirschmann (2000), the theoretical solidus of normal peridotite is 1248·5°C at 1·0 GPa and 1223·7°C at 0·8GPa. Assuming a similar pressure dependence, the theoretical solidus of BaSC at 0·8 GPa would thus be 1261·5°C. However, because of the chemically and texturally unequilibrated nature of BaSC, the actual solidus might differ. Nonetheless, the 15 h dry melting run on BaSC2 resulted in a mineral mode very similar to initial BaSC and ~2 area % of melt-filled porosity (Fig. 3b). As the initial porosity of our starting mix after hipping is higher at ~6 area %, this testifies that 1260°C is close to the dry solidus of our peridotite mix.

The PL modal compositions for reaction experiments conducted with two different starting liquid compositions (HK#19 and HK#20, respectively) are displayed in Fig. 3c and d. The modal variability of opx and olivine in 1200°C runs exemplifies initial PL heterogeneity as there is hardly any evidence (textural or compositional) for reaction. The same holds true for runs at 1230°C (GB06 and

GB41). At higher temperatures, there is a trend towards increasing amounts of melt at the expense of spinel and pyroxene, whereas olivine modes remain variable as a result of initial heterogeneity. Figure 3c reveals overlapping modes within (heterogeneity-induced) error for experiments involving HK#19.1 and HK#19.v. In reaction with HK#19, 4–5 vol. % cpx persists at 1260°C, whereas cpx is completely consumed by reaction in HK#20 at $T > \sim$1240°C. Opx fractions decrease from the initial value of ~25 vol. % to ~14 vol. % at 1290°C for both starting liquid compositions. There is a general decrease of modal opx with increasing temperature, but significant variations also occur as a result of initial PL heterogeneity. Melt fractions start to rise at temperatures above 1230°C, with a constant increase from ~6 vol. % at 1230°C to ~14 vol. % at 1260°C and to ~22 vol. % at 1290°C.

Mineral compositions

Detailed measurements were undertaken for all recovered charges to investigate compositional changes related to melt–peridotite reaction. Averaged phase compositions from selected runs are given in Table 4. Data for melt and peridotite layers are listed separately, with a further split between (inherited) core and (new) rim compositions for the PL data. As newly precipitated phases in PL melt pockets and equilibrated rims of original grains have overlapping compositions, they are grouped together under the term 'rim'. Additionally, the compositional data are presented as grain-scale to charge-scale compositional profiles and illustrated in variation diagrams (Figs 4–9). Single-grain profiles were carefully evaluated with respect to secondary fluorescence contamination (e.g. Llovet & Galan, 2003). To minimize the latter effect, and to increase the probability of measuring a profile through an inner core, we generally selected the largest grains and/or grains with best-developed rims.

Olivine

Olivine becomes chemically more equilibrated with progressively higher run temperature and longer run durations. This is expressed by a reduction of compositional variation, both on a larger scale between ML and PL olivine grains and on a single-grain level between (remnant) cores and rims (Table 4, Figs 4 and 5). Generally, newly formed olivine and equilibrated rims show enrichment in Ca and Cr and depletion in Ni. The Mg-number of newly formed olivine decreases from 0·92 at 1290°C to as low as 0·85 at 1200°C. Up to 1230°C, there is a clear Fe-enrichment and Mg-depletion from inherited cores towards rims. Figure 4 shows the FeO and MgO contents of olivine cores as a function of distance to the ML–PL interface for one run at 1290°C and two runs at 1200°C (15 h, 92 h). The flat profile at 1290°C shows complete equilibration over the length of the capsule. In contrast, both 1200°C runs display downward trends for FeO and upward trends for MgO from the ML towards the PL, approaching the original San Carlos composition. Not surprisingly, the 92 h run exhibits flatter profiles than the 15 h run and thus advanced equilibration. Figure 5 displays CaO and Mg-number profiles for single olivine grains at variable distances into the PL for runs at 1200°C and 1290°C, respectively. Olivine shows continuous rim-to-rim zoning, again with flatter profiles at higher T as a result of more advanced equilibration. The '0 μm' grain in GB35 exhibits an asymmetric zoning pattern as a result of being in direct contact with the ML liquid at one side and in contact with a PL melt pocket at the opposing side. This is, in addition, the only olivine grain analyzed in GB35 that contains a core composition significantly different from the initial San Carlos olivine. Continuous zoning trends such as those displayed here are indicative of diffusive equilibration (see Discussion). Figure 5 furthermore illustrates that Fe–Mg interdiffusion is faster than Ca diffusion in olivine, as confirmed by several studies on cation diffusion in olivine (e.g. Jurewicz & Watson, 1988).

Pyroxenes

Pyroxenes commonly reveal inherited cores and newly grown rims or precipitates with distinctly different compositions (Table 4, Figs 6 and 7). Newly formed cpx is generally enriched in Mg, Fe (but nevertheless with lower Mg-number) and Mn, and depleted in Ca, Na and Ti, compared with the starting Balmuccia cpx. Cpx coexisting with melt at the run conditions exhibits increasing Cr/Al with increasing temperature (Table 4). Inherited cores in the PL still retain their initial composition for all elements except for Fe, Mg and Na. For these three elements, the compositional shift increases with temperature (see Table 4). Newly formed opx is enriched in Al, Ca, Cr, Ti and Na, and depleted in Fe, Mg and Si relative to the starting Balmuccia opx. Inherited opx cores retain the initial Balmuccia composition for all elements. As for olivine, newly precipitated/well-equilibrated cpx (from 0·91 to 0·86) and opx (from 0·92 to 0·86) show a progressive decrease in Mg-number as run temperature decreases from 1290°C to 1200°C. Compositional profiles across an opx and a cpx grain are illustrated in Fig. 6. In contrast to olivine, both pyroxenes display discontinuous zoning with a sharp compositional step between core and rim, indicating that dissolution–reprecipitation is the dominant mechanism of rim formation. Inherited cores show very little or no compositional variation, whereas rims can be slightly heterogeneous. Figure 7 illustrates ML, PL core and PL rim pyroxene compositions as a function of temperature and starting composition. PL cores show weak compositional shifts with respect to Balmuccia pyroxene, as opposed to PL rims and ML precipitates. Both opx and cpx have higher Al contents in MLs and their respective PLs.

Table 4: Electron microprobe analyses of run products from selected runs in wt %

Run	*	*n*		SiO_2	TiO_2	Cr_2O_3	Al_2O_3	FeO_{tot}	MnO	NiO	MgO	CaO	Na_2O	K_2O	Total	Mg-no.	X_{An}	Cr-no.	Cr/Al
With HK#19 starting composition																			
GB14																			
Ol	ML	1		39·41	0·02	—	0·09	14·37	0·20	—	44·17	0·38	—	—	98·7	0·85			
	PL R	10	Av	40·39	0·02	0·09	0·06	10·93	0·22	0·29	47·55	0·24	—	—	99·7	0·89			
			SD	0·59	0·01	0·06	0·04	1·85	0·09	0·11	1·67	0·04	—	—	0·67	0·02			
	PL C	15	Av	40·79	0·01	0·04	0·04	10·54	0·16	0·32	48·01	0·11	—	—	100·0	0·89			
			SD	0·55	0·01	0·01	0·01	1·42	0·03	0·10	1·29	0·03	—	—	0·72	0·02			
Opx	ML	4	Av	53·30	0·21	0·50	4·71	8·50	0·21	—	29·01	2·74	0·03	—	99·2	0·86			
			SD	0·42	0·02	0·12	0·91	0·30	0·06	—	0·39	0·23	0·01	—	0·10	0·01			
	PL R	4	Av	56·14	0·10	0·50	2·87	6·38	0·12	0·12	32·02	1·67	0·07	—	100·0	0·90			
			SD	0·74	0·02	0·04	0·33	0·12	0·05	0·04	0·46	0·44	0·04	—	0·74	0·00			
	PL C	23	Av	56·05	0·07	0·47	3·00	6·05	0·15	0·12	33·62	0·44	0·03	—	100·0	0·91			
			SD	0·68	0·01	0·11	0·45	0·25	0·03	0·06	0·35	0·12	0·02	—	0·81	0·00			
Cpx	ML	5	Av	51·31	0·51	0·60	6·11	6·31	0·16	0·05	19·03	14·97	0·21	—	99·2	0·84			0·07
			SD	0·66	0·19	0·14	1·28	0·72	0·09	0·00	1·24	0·83	0·06	—	0·43	0·02			0·01
	PL R	10	Av	52·91	0·29	0·94	4·68	4·09	0·13	0·11	19·45	16·73	0·41	—	99·7	0·89			0·14
			SD	0·85	0·05	0·19	1·08	0·40	0·04	0·06	2·04	1·95	0·12	—	0·79	0·01			0·05
	PL C	11	Av	53·01	0·26	1·08	4·34	2·71	0·08	0·13	16·23	21·87	0·65	—	100·3	0·91			0·17
			SD	0·66	0·02	0·16	0·36	0·55	0·03	0·05	0·95	1·24	0·20	—	0·88	0·01			0·03
Sp	PL C	13	Av	0·02	0·13	25·86	41·48	16·51	—	0·15	15·21	0·04	—	—	99·4	0·64		0·29	0·42
			SD	0·02	0·01	0·80	1·14	1·46	—	0·10	0·34	0·02	—	—	0·91	0·02		0·01	0·02
Plg	ML	4	Av	47·16	0·05	—	32·88	0·48	—	—	0·41	15·76	1·27	0·03	98·2		0·87		
			SD	0·87	0·01	—	1·11	0·08	—	—	0·13	0·44	0·14	0·01	0·37		0·02		
Melt	MT†	12	Av	55·66	0·44	0·11	17·04	3·52	0·08	—	4·57	8·54	2·41	0·27	92·7	0·70			
			SD	1·36	0·02	0·09	0·23	0·46	0·07	—	0·54	0·60	0·20	0·04	0·64	0·01			
	PL	25	Av	50·65	0·73	0·24	18·05	5·70	0·13	—	4·84	10·73	2·02	0·24	93·4	0·60			
			SD	0·80	0·22	0·20	0·59	0·32	0·09	—	0·64	0·81	0·17	0·04	0·80	0·03			
GB06																			
Ol	ML	11	Av	40·93	—	0·10	0·08	10·06	0·15	0·17	48·52	0·23	—	—	100·3	0·90			
			SD	0·27	—	0·02	0·04	0·23	0·02	0·05	0·20	0·07	—	—	0·37	0·00			
	PL R	8	Av	41·13	—	0·17	0·05	9·61	0·15	0·31	49·21	0·24	—	—	100·9	0·90			
			SD	0·30	—	0·06	0·01	0·41	0·01	0·07	0·63	0·02	—	—	0·67	0·00			
	PL C	37	Av	41·27	—	0·09	0·04	9·09	0·14	0·34	49·62	0·12	—	—	100·7	0·91			
			SD	0·23	—	0·05	0·01	0·54	0·02	0·08	0·56	0·04	—	—	0·43	0·01			
Opx	PL R	6	Av	56·84	0·07	0·68	2·14	5·85	0·14	0·14	33·01	1·89	0·07	—	100·8	0·91			
			SD	0·62	0·02	0·25	0·76	0·26	0·01	0·03	0·60	0·44	0·01	—	0·29	0·00			
	PL C	33	Av	57·12	0·06	0·31	2·19	6·24	0·15	0·13	34·19	0·46	0·04	—	100·8	0·91			
			SD	0·76	0·01	0·17	1·04	0·24	0·02	0·04	0·59	0·21	0·01	—	0·34	0·00			
Cpx	ML	2	Av	50·81	0·24	1·06	7·41	3·92	0·13	0·03	19·00	15·79	0·23	—	98·6	0·90			0·10
			SD	1·08	0·02	0·01	0·28	0·10	0·02	0·03	0·41	0·76	0·01	—	0·35	0·00			0·00
	PL R	7	Av	53·47	0·15	1·42	3·85	3·46	0·10	0·12	20·14	17·56	0·34	—	100·6	0·91			0·25
			SD	0·60	0·03	0·38	0·78	0·27	0·02	0·04	0·68	1·18	0·06	—	0·44	0·00			0·03
	PL C	24	Av	52·95	0·22	1·13	4·66	3·17	0·10	0·10	17·65	19·67	0·59	—	100·2	0·91			0·18
			SD	0·86	0·09	0·24	1·66	0·90	0·03	0·04	2·01	3·30	0·19	—	0·85	0·02			0·07
Sp	PL R	8	Av	0·20	0·20	38·22	32·76	10·15	—	0·19	17·93	0·11	—	—	99·7	0·76		0·44	0·79
			SD	0·17	0·01	2·28	2·27	0·21	—	0·05	0·46	0·06	—	—	0·88	0·01		0·03	0·11
	PL C	20	Av	0·05	0·13	30·53	36·16	18·07	—	0·18	14·34	0·02	0·04	—	99·5	0·62		0·35	0·57
			SD	0·03	0·01	0·91	1·22	2·48	—	0·06	1·27	0·01	0·01	—	0·46	0·05		0·01	0·03
Melt	ML	5	Av	48·65	0·62	0·15	17·54	6·73	0·17	—	10·13	12·08	1·56	0·07	97·7	0·73			
			SD	0·29	0·02	0·04	0·15	0·37	0·05	—	0·24	0·15	0·03	0·01	0·59	0·01			
	PL	17	Av	50·72	0·59	0·31	17·37	6·14	0·14	—	7·05	12·67	1·89	0·13	97·1	0·67			
			SD	0·65	0·08	0·11	0·86	0·53	0·03	—	0·91	0·40	0·14	0·02	0·47	0·03			
GB08																			
Ol	ML	19	Av	41·11	—	0·40	0·06	8·62	0·13	0·08	49·39	0·26	—	—	100·0	0·91			
			SD	0·32	—	0·07	0·01	0·12	0·01	0·08	0·27	0·05	—	—	0·51	0·00			
	PL	7	Av	40·58	—	0·47	0·05	8·23	0·11	0·07	49·44	0·28	—	—	99·3	0·91			
			SD	0·23	—	0·06	0·02	0·14	0·01	0·07	0·37	0·04	—	—	0·38	0·00			

(continued)

Table 4: Continued

Run	*	*n*		SiO_2	TiO_2	Cr_2O_3	Al_2O_3	FeO_{tot}	MnO	NiO	MgO	CaO	Na_2O	K_2O	Total	Mg-no.	X_{An}	Cr-no.	Cr/Al
GB08																			
Opx	PL	R	9	Av	56·23	0·05	1·11	1·58	5·28	0·13	0·12	32·65	2·14	0·05	—	99·3	0·92			
				SD	0·40	0·02	0·17	0·19	0·22	0·02	0·05	0·33	0·14	0·01	—	0·50	0·00			
	PL	C	16	Av	56·05	0·07	0·47	2·74	5·91	0·14	0·11	33·65	0·37	0·03	—	99·5	0·91			
				SD	0·20	0·01	0·11	0·30	0·16	0·01	0·03	0·17	0·08	0·01	—	0·30	0·00			
Sp	ML		11	Av	0·24	0·23	46·80	24·45	10·08	—	—	17·06	0·19	—	—	99·1	0·75		0·56	1·28
				SD	0·09	0·01	0·44	0·27	0·14	—	—	0·18	0·02	—	—	0·80	0·00		0·00	0·01
	PL	R	16	Av	0·18	0·18	53·22	18·43	10·63	—	0·14	16·26	0·16	0·05	—	99·2	0·74		0·65	1·96
				SD	0·04	0·03	2·11	1·61	0·20	—	0·04	0·33	0·03	0·02	—	0·73	0·01		0·03	0·24
Melt	ML		15	Av	49·83	6·43	0·05	1·13	0·14	13·66	0·48	12·44	0·57	12·19	0·01	96·9	0·78			
				SD	0·31	0·24	0·01	0·04	0·03	0·16	0·02	0·14	0·06	0·08	0·02	0·53	0·01			
	PL		43	Av	51·16	6·54	0·06	1·26	0·15	14·16	0·47	8·76	0·63	13·37	0·02	96·6	0·71			
				SD	0·82	0·40	0·01	0·11	0·02	1·22	0·08	2·25	0·10	0·86	0·02	0·80	0·05			
GB40																				
Ol	ML		15	Av	40·76	—	0·42	0·06	8·73	0·14	—	50·65	0·30	—	—	101·1	0·90			
				SD	0·17	—	0·03	0·02	0·08	0·02	—	0·23	0·04	—	—	0·37	0·00			
	PL		12	Av	40·93	—	0·47	0·07	8·76	0·15	0·05	50·50	0·33	—	—	101·3	0·90			
				SD	0·16	—	0·02	0·01	0·06	0·02	0·06	0·09	0·02	—	—	0·20	0·00			
Opx	PL	R	5	Av	55·74	0·09	1·07	2·92	5·39	0·14	—	32·71	2·79	0·06	—	101·0	0·92			
				SD	0·49	0·02	0·31	0·47	0·23	0·02	—	0·89	1·03	0·01	—	0·20	0·00			
	PL	C	18	Av	56·68	0·06	0·32	2·21	6·00	0·15	0·09	34·95	0·48	0·04	—	100·9	0·91			
				SD	0·40	0·01	0·16	0·64	0·16	0·01	0·02	0·45	0·39	0·01	—	0·22	0·00			
Cpx	ML		2	Av	52·52	0·19	1·70	4·74	3·90	0·14	—	21·80	14·93	0·24	—	100·2	0·91			0·24
				SD	0·07	0·01	0·06	0·11	0·02	0·00	—	0·34	0·22	0·00	—	0·18	0·01			0·00
	PL	R	10	Av	53·71	0·15	1·39	3·91	4·33	0·13	—	23·98	12·63	0·21	—	100·5	0·91			0·24
				SD	0·66	0·02	0·14	0·55	0·22	0·02	—	1·11	1·20	0·03	—	0·25	0·00			0·02
	PL	C	3	Av	52·74	0·27	1·11	4·47	2·70	0·09	—	16·72	22·03	0·50	—	100·7	0·92			0·17
				SD	0·29	0·01	0·02	0·09	0·04	0·01	—	0·29	0·28	0·03	—	0·21	0·00			0·00
Sp	PL	R	2	Av	0·15	0·17	34·46	37·21	9·11	—	—	19·05	0·09	—	—	100·3	0·79		0·38	0·62
				SD	0·01	0·01	0·75	1·00	0·14	—	—	0·06	0·02	—	—	0·01	0·00		0·01	0·03
	PL	C	37	Av	0·05	0·19	24·35	43·19	15·51	0·05	0·20	16·35	0·09	0·05	—	100·0	0·67		0·27	0·38
				SD	0·03	0·03	0·43	1·60	2·84	0·02	0·06	1·62	0·04	0·04	—	1·06	0·05		0·00	0·01
Melt	ML		15	Av	50·12	0·56	0·59	15·38	6·49	0·14	—	12·03	12·63	1·40	0·07	99·5	0·77			
				SD	0·27	0·02	0·02	0·17	0·12	0·03	—	0·24	0·16	0·08	0·01	0·33	0·01			
	PL		43	Av	50·65	0·50	0·56	16·23	6·82	0·14	—	9·36	13·52	1·44	0·06	99·3	0·71			
				SD	0·46	0·05	0·17	0·69	0·37	0·03	—	1·36	0·44	0·17	0·01	0·48	0·03			
GB41																				
Ol	ML		12	Av	40·47	0·01	0·21	0·07	10·64	0·19	—	49·20	0·35	—	—	101·2	0·88			
				SD	0·14	0·01	0·01	0·03	0·08	0·02	—	0·20	0·04	—	—	0·19	0·00			
	PL	R	8	Av	40·84	—	0·18	0·06	9·71	0·15	0·24	49·85	0·28	—	—	101·3	0·89			
				SD	0·12	—	0·02	0·03	0·54	0·03	0·09	0·54	0·03	—	—	0·23	0·01			
	PL	C	47	Av	40·85	—	0·11	0·04	9·18	0·14	0·32	50·55	0·14	—	—	101·3	0·90			
				SD	0·17	—	0·04	0·01	0·60	0·02	0·09	0·54	0·05	—	—	0·21	0·01			
Opx	PL	R	6	Av	55·17	0·10	0·67	4·10	5·67	0·14	0·12	32·34	2·58	0·07	—	100·9	0·91			
				SD	0·28	0·02	0·16	0·55	0·08	0·02	0·06	0·55	0·30	0·04	—	0·31	0·00			
	PL	C	41	Av	56·23	0·08	0·43	2·80	6·17	0·15	0·13	34·58	0·45	0·04	—	101·0	0·91			
				SD	0·51	0·01	0·15	0·68	0·15	0·02	0·04	0·42	0·29	0·01	—	0·22	0·00			
Cpx	ML		12	Av	51·82	0·29	1·26	5·92	4·26	0·17	—	20·21	16·10	0·27	—	100·3	0·89			0·14
				SD	0·62	0·04	0·18	0·42	0·31	0·02	—	0·90	1·07	0·02	—	0·33	0·00			0·02
	PL	R	8	Av	52·27	0·23	1·17	5·34	4·04	0·12	—	20·56	16·37	0·27	—	100·5	0·90			0·15
				SD	0·63	0·05	0·22	0·76	0·32	0·01	—	1·06	1·11	0·03	—	0·21	0·00			0·01
	PL	C	22	Av	52·72	0·28	1·13	4·40	2·76	0·08	—	16·77	21·79	0·61	—	100·6	0·92			0·17
				SD	0·37	0·02	0·11	0·28	0·39	0·03	—	0·94	1·27	0·14	—	0·27	0·01			0·01
Sp	PL	C	30	Av	0·05	0·09	23·27	44·05	16·18	—	0·14	16·57	0·04	—	—	100·5	0·68		0·25	0·36
				SD	0·02	0·04	2·07	2·57	3·83	—	0·09	1·83	0·02	—	—	0·47	0·06		0·02	0·05
Plg	ML		12	Av	49·30	0·05	0·03	31·88	0·42	0·02	—	0·57	15·31	2·61	0·03	100·2	0·68	0·76		
				SD	0·29	0·03	0·01	0·75	0·16	0·01	—	0·38	0·18	0·06	0·01	0·38	0·06	0·01		

(continued)

Table 4: Continued

Run	*	*n*		SiO_2	TiO_2	Cr_2O_3	Al_2O_3	FeO_{tot}	MnO	NiO	MgO	CaO	Na_2O	K_2O	Total	Mg-no.	X_{An}	Cr-no.	Cr/Al
Melt	ML	16	Av	49·83	0·79	0·14	18·04	7·17	0·17	—	8·50	11·73	2·16	0·13	98·7	0·68			
			SD	0·41	0·04	0·06	0·69	0·21	0·02	—	1·15	0·17	0·20	0·02	0·38	0·03			
	PL	32	Av	50·42	0·61	0·25	18·05	6·27	0·14	—	8·57	12·23	2·11	0·12	98·8	0·71			
			SD	0·40	0·08	0·09	0·51	0·31	0·03	—	0·91	0·56	0·13	0·01	0·46	0·02			
With HK#20 starting composition																			
GB33																			
Ol	ML	12	Av	40·71	0·02	0·22	0·08	8·78	0·14	—	49·36	0·37	—	—	99·7	0·91			
			SD	0·15	0·01	0·01	0·01	0·13	0·01	—	0·15	0·02	—	—	0·23	0·00			
	PL R	7	Av	40·84	—	0·23	0·08	8·86	0·14	0·27	49·53	0·33	—	—	100·3	0·90			
			SD	0·21	—	0·02	0·02	0·04	0·02	0·11	0·18	0·03	—	—	0·24	0·00			
	PL C	28	Av	40·75	—	0·20	0·04	8·85	0·13	0·21	49·69	0·24	—	—	100·2	0·90			
			SD	0·20	—	0·02	0·01	0·15	0·02	0·12	0·23	0·04	—	—	0·34	0·00			
Opx	ML	19	Av	54·22	0·10	1·00	4·57	5·29	0·13	0·08	31·28	2·88	0·05	—	99·6	0·91			
			SD	0·29	0·01	0·12	0·34	0·14	0·01	0·01	0·32	0·35	0·02	—	0·39	0·00			
	PL R	5	Av	55·24	0·07	0·84	3·54	5·43	0·13	—	31·96	2·73	0·05	—	100·0	0·91			
			SD	0·30	0·01	0·10	0·57	0·11	0·02	—	0·35	0·16	0·02	—	0·36	0·00			
	PL C	27	Av	55·98	0·06	0·46	3·03	5·95	0·14	0·11	33·77	0·57	0·04	—	100·0	0·91			
			SD	0·39	0·01	0·09	0·29	0·19	0·02	0·03	0·31	0·34	0·01	—	0·32	0·00			
Cpx	ML	6	Av	51·91	0·17	1·31	5·71	3·97	0·13	—	21·61	14·48	0·19	—	99·5	0·91			0·10
			SD	0·31	0·02	0·03	0·22	0·16	0·02	—	0·81	0·84	0·03	—	0·28	0·00			0·00
	PL R	9	Av	53·37	0·11	1·04	4·35	4·36	0·13	—	23·35	13·14	0·19	—	100·1	0·91			0·10
			SD	0·81	0·03	0·22	0·68	0·28	0·02	—	1·24	1·18	0·01	—	0·51	0·00			0·00
	PL C	27	Av	52·60	0·24	1·02	4·54	2·77	0·08	0·13	16·92	21·05	0·64	—	99·9	0·92			0·09
			SD	0·68	0·06	0·11	0·68	0·61	0·02	0·06	2·58	3·01	0·18	—	0·47	0·01			0·01
Sp	PL R	1		0·17	0·14	35·16	36·41	9·41	—	0·18	18·55	0·13	0·04	—	100·2	0·77		0·39	0·65
	PL C	24	Av	0·11	0·13	26·62	41·33	14·46	—	0·16	16·91	0·09	—	—	99·8	0·70		0·30	0·44
			SD	0·07	0·02	1·82	2·81	2·98	—	0·09	1·37	0·03	—	—	0·55	0·05		0·02	0·06
Melt	ML	19	Av	49·43	0·51	0·22	16·23	6·73	0·16	—	10·70	13·04	1·22	0·05	98·3	0·74			
			SD	0·33	0·02	0·06	0·45	0·29	0·03	—	0·82	0·27	0·09	0·01	0·36	0·02			
	PL	33	Av	49·59	0·48	0·26	16·93	7·17	0·14	—	8·62	13·44	1·29	0·05	98·0	0·68			
			SD	0·67	0·05	0·16	0·88	0·57	0·03	—	1·42	0·66	0·15	0·01	0·92	0·04			
GB34																			
Ol	ML	19	Av	41·19	0·01	0·29	0·09	8·82	0·14	—	49·83	0·38	—	—	100·8	0·90			
			SD	0·12	0·01	0·02	0·04	0·09	0·02	—	0·37	0·03	—	—	0·36	0·00			
	PL R	10	Av	41·20	—	0·37	0·06	8·82	0·13	0·17	49·41	0·36	—	—	100·5	0·90			
			SD	0·14	—	0·04	0·02	0·07	0·01	0·11	0·14	0·04	—	—	0·19	0·00			
	PL C	42	Av	41·13	—	0·24	0·04	8·80	0·13	0·22	49·57	0·22	—	—	100·4	0·90			
			SD	0·14	—	0·09	0·02	0·12	0·02	0·13	0·20	0·06	—	—	0·21	0·00			
Opx	ML	6	Av	54·99	0·13	0·91	4·53	5·55	0·14	—	31·39	2·42	—	—	100·1	0·91			
			SD	0·46	0·03	0·19	0·37	0·18	0·02	—	0·44	0·42	—	—	0·43	0·00			
	PL R	10	Av	55·29	0·12	0·84	4·05	5·80	0·14	—	31·47	2·38	—	—	100·2	0·91			
			SD	0·43	0·03	0·19	0·47	0·49	0·02	—	0·36	0·38	—	—	0·24	0·01			
	PL C	42	Av	56·75	0·07	0·33	2·42	6·03	0·15	—	33·98	0·49	—	—	100·3	0·91			
			SD	0·28	0·01	0·07	0·36	0·13	0·02	—	0·28	0·35	—	—	0·26	0·00			
Cpx	PL R	5	Av	53·91	0·11	1·12	3·67	4·13	0·13	—	22·54	14·34	0·16	—	100·2	0·91			0·21
			SD	0·53	0·01	0·12	0·36	0·22	0·01	—	1·11	1·47	0·03	—	0·13	0·00			0·03
	PL C	30	Av	52·95	0·23	1·15	4·58	3·12	0·08	—	17·83	19·62	0·44	—	100·1	0·91			0·17
			SD	0·44	0·06	0·09	0·68	0·67	0·02	—	2·21	2·96	0·19	—	0·31	0·01			0·02
Sp	PL C	12	Av	0·07	0·12	24·50	43·49	13·46	—	0·18	17·25	0·07	—	—	99·2	0·71		0·27	0·38
			SD	0·03	0·01	0·30	1·15	2·77	—	0·08	1·37	0·02	—	—	0·17	0·05		0·00	0·01
Melt	ML	16	Av	50·02	0·52	0·31	15·46	6·72	0·14	—	11·22	12·89	1·15	0·04	98·5	0·75			
			SD	0·33	0·02	0·07	0·30	0·26	0·03	—	0·85	0·16	0·09	0·01	0·49	0·02			
	PL	25	Av	50·53	0·45	0·44	15·58	6·77	0·14	—	10·10	13·49	1·05	0·04	98·7	0·72			
			SD	0·47	0·07	0·08	0·59	0·26	0·02	—	1·32	0·57	0·07	0·01	0·34	0·03			
GB35																			
Ol	ML	5	Av	39·92	0·03	0·12	0·15	13·65	0·20	—	45·81	0·38	—	—	100·3	0·85			
			SD	0·12	0·01	0·03	0·06	0·10	0·01	—	0·11	0·03	—	—	0·20	0·00			

(continued)

Table 4: Continued

Run	*	*n*		SiO_2	TiO_2	Cr_2O_3	Al_2O_3	FeO_{tot}	MnO	NiO	MgO	CaO	Na_2O	K_2O	Total	Mg-no.	X_{An}	Cr-no.	Cr/Al
GB35																			
Ol	PL	R	12	Av	40·63	—	0·10	0·07	10·07	0·15	0·28	48·86	0·25	—	—	100·4	0·89			
				SD	0·40	—	0·03	0·05	1·52	0·03	0·18	1·22	0·06	—	—	0·27	0·02			
	PL	C	49	Av	40·83	—	0·07	0·04	9·45	0·14	0·33	49·52	0·12	—	—	100·5	0·90			
				SD	0·30	—	0·02	0·01	1·06	0·02	0·13	0·81	0·04	—	—	0·41	0·01			
Opx	ML		2	Av	53·91	0·39	0·53	4·79	8·40	0·19	—	29·23	2·63	0·09	0·01	100·2	0·86			
				SD	0·01	0·04	0·00	0·31	0·14	0·01	—	0·54	0·41	0·04	0·00	0·22	0·00			
	PL	R	8	Av	55·32	0·07	0·23	1·78	6·42	0·16	—	32·97	0·91	0·05	—	98·0	0·90			
				SD	2·72	0·02	0·09	0·55	0·68	0·02	—	1·64	0·09	0·01	—	4·90	0·01			
	PL	C	19	Av	56·69	0·07	0·25	1·74	6·31	0·15	0·15	34·20	0·51	—	—	100·0	0·91			
				SD	0·67	0·01	0·15	0·61	0·34	0·02	0·05	0·55	0·27	—	—	0·72	0·01			
Cpx	ML		3	Av	51·56	0·47	0·75	5·84	5·55	0·16	—	18·77	16·47	0·24	0·02	99·9	0·86			0·09
				SD	0·61	0·15	0·13	0·31	0·31	0·03	—	0·88	0·50	0·02	0·02	0·56	0·01			0·02
	PL	R	17	Av	52·55	0·27	0·89	4·85	3·44	0·10	0·09	19·01	18·70	0·25	—	100·2	0·91			0·13
				SD	0·45	0·04	0·11	0·58	0·53	0·03	0·08	1·96	2·84	0·03	—	0·36	0·01			0·02
	PL	C	39	Av	52·59	0·29	1·07	4·34	2·66	0·07	0·05	16·33	22·01	0·58	—	100·0	0·92			0·17
				SD	0·28	0·02	0·13	0·25	0·22	0·02	0·06	0·79	1·07	0·14	—	0·32	0·00			0·02
Sp	PL	C	40	Av	0·05	0·17	24·67	42·74	15·80	—	0·20	16·42	0·04	—	—	100·1	0·68		0·27	0·39
				SD	0·02	0·03	0·24	1·29	2·82	—	0·06	1·32	0·03	—	—	0·34	0·05		0·00	0·01
Plg	ML		4	Av	47·69	0·10	—	31·07	0·75	—	—	1·37	15·78	2·00	0·03	98·8	0·75	0·81		
				SD	0·84	0·04	—	1·14	0·21	—	—	0·58	0·15	0·07	0·01	1·08	0·04	0·00		
	PL		2	Av	48·72	—	—	31·93	0·55	—	—	0·36	15·37	2·48	0·02	99·5	0·54	0·77		
				SD	0·40	—	—	0·35	0·04	—	—	0·01	0·21	0·12	0·00	0·07	0·01	0·01		
Melt	MT†		14	Av	51·37	0·59	0·08	17·66	6·04	0·11	—	8·41	11·78	1·74	0·12	98·0	0·71			
				SD	1·14	0·04	0·02	0·47	0·24	0·02	—	0·49	0·16	0·15	0·02	0·38	0·01			
	PL		21	Av	49·87	0·83	0·11	18·79	5·97	0·13	—	8·00	11·87	2·12	0·12	97·9	0·70			
				SD	0·77	0·24	0·04	0·89	0·36	0·03	—	1·32	0·61	0·25	0·02	0·97	0·03			
GB37																				
Ol	ML		6	Av	40·83	—	0·43	0·07	8·16	0·14	—	49·79	0·31	—	—	99·8	0·92			
				SD	0·11	—	0·02	0·01	0·04	0·03	—	0·14	0·01	—	—	0·20	0·00			
	PL	R	27	Av	40·61	—	0·49	0·06	8·36	0·12	0·13	49·67	0·29	—	—	99·7	0·91			
				SD	0·25	—	0·03	0·02	0·09	0·01	0·03	0·20	0·01	—	—	0·31	0·00			
	PL	C	37	Av	40·63	—	0·47	0·05	8·33	0·12	0·15	49·70	0·24	—	—	99·7	0·91			
				SD	0·24	—	0·03	0·01	0·07	0·01	0·05	0·13	0·03	—	—	0·25	0·00			
Opx	PL	R	14	Av	56·21	0·05	0·94	2·13	5·23	0·13	0·11	32·82	2·23	0·04	—	99·8	0·92			
				SD	0·40	0·01	0·17	0·49	0·12	0·01	0·03	0·34	0·60	0·01	—	0·23	0·00			
	PL	C	26	Av	55·98	0·07	0·46	2·92	5·92	0·14	0·11	33·78	0·41	0·03	—	99·8	0·91			
				SD	0·59	0·01	0·16	0·47	0·20	0·02	0·04	0·27	0·24	0·01	—	0·26	0·00			
Melt	ML		14	Av	50·09	0·44	0·57	13·87	6·91	0·15	—	13·28	11·90	0·88	0·03	98·2	0·77			
				SD	0·25	0·03	0·04	0·15	0·17	0·04	—	0·56	0·31	0·07	0·01	0·26	0·01			
	PL		21	Av	50·84	0·42	0·63	14·44	7·03	0·16	—	10·19	13·14	0·93	0·03	97·9	0·72			
				SD	0·62	0·04	0·13	0·88	0·31	0·03	—	1·83	0·71	0·12	0·01	0·51	0·04			

Dashes indicate that the element was below or close to (more than half of the analyses below) the detection limit.
*Phase analyses for the PL domain were separated in inherited 'core' (C) and new 'rim' (R) compositions, based on Ca content for ol, opx and cpx, and on Cr-number for spinel.
†Average for the MT domain is given and used in element partition coefficient calculations (see Table 5), as quench crystallization affected the ML domain severely.
ML, melt layer; PL, peridotite layer; MT, melt trap; *n*, number of analyses; Av, average; SD, standard deviation.

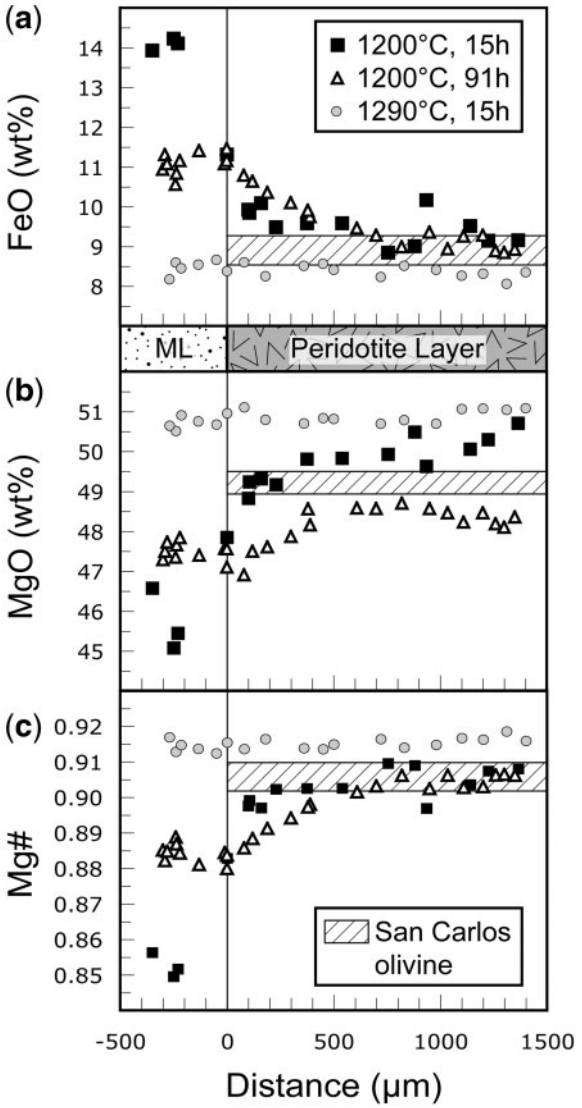

Fig. 4. Olivine FeO (a) and MgO (b) core contents (in wt %) and Mg-number (c) as a function of distance to the ML–PL interface for one run at 1290°C and two runs at 1200°C performed with different run times (15 h vs 92 h).

Spinel

Spinel in equilibrium with melt at run conditions is generally enriched in Al and Mg and depleted in (total and calculated) Fe^{2+} and calculated Fe^{3+}. Figure 8 reveals multiple equilibration processes for the 1230°C spinel grain shown in Fig. 2. This spinel grain records continuous trends of decreasing Fe and increasing Mg, and discontinuous trends for Al and Cr. Sharp Al decrease and Cr increase occur at the interface between a partly dissolved (rounded) inherited core and a newly grown rim. In contrast, continuous Fe and Mg zoning trends extend over both generations of spinel. Furthermore, the core area exhibits a small increase of Al towards the interface with the reprecipitated rim. This is a general feature observed for inherited spinel cores in our runs, with the increase in Al^{3+} per formula unit being equal to the decrease of calculated Fe^{3+}, thus indicating a coupled substitution diffusion mechanism. Figure 9 illustrates Mg-number and TiO_2 contents as a function of Cr-number. At 1200°C, spinel shows equilibration towards higher Mg-numbers and TiO_2 at constant (initial) Cr-number. At 1230–1250°C there is, in addition to the Mg-number and TiO_2 variation, also a continuous spread in Cr-number between initial values and values up to ~0·50. Significant increase in Cr-number occurs only in reprecipitated rims. At 1260°C, the spread in Mg-number and TiO_2 persists, and the range in Cr-number is extended up to ~0·7. At 1290°C, complete dissolution of initial cores and limited reprecipitation (only in HK#19.1 experiments) results in smaller variation in Mg-number (~0·72) and TiO_2 (~0·2), at Cr-numbers between 0·56 and 0·7.

Plagioclase

Plagioclase in the 1200°C HK#19.1 and HK#20 runs, and in the 1230°C HK#19.v run (GB41) is bytownitic ($An_{77–81}$) in composition, with negligible amounts of K_2O ($\leq$0·05 wt %). This is similar to the highest-T plagioclase in the crystallization experiments of Villiger *et al.* (2004, 2007).

Mineral–liquid equilibria

To evaluate the extent of equilibration between melt and peridotite solid phase–liquid partition coefficients were calculated following the same technique of separation into ML, PL core and PL rim phase compositions as for the solid phases (see above). The averaged ML and PL melt compositions used for the mineral–liquid K_D calculations are given in Table 4. As quench modification affects (smaller) melt pools in PLs considerably more than ML liquids, average ML compositions were mostly used for these calculations. At temperatures below 1260°C, where the amount of melt in MLs decreases, quenching can also affect the ML composition extensively. This is especially true for Fe and Mg as a result of olivine quench crystallization. Consequently, we selected MT compositions to calculate D values for these elements (see Table 5). Furthermore, TiO_2 contents in glasses consistently decrease from the ML to the MT, reflecting the higher TiO_2 of the starting liquid. Therefore, D_{Ti} values for PL cpx–liquid averages were calculated using the average TiO_2 contents of PL glasses. A variety of mineral–liquid distribution coefficients for selected runs are given in Table 5. In the following discussion, we mostly list ranges (means $\pm 1\sigma$) to improve readability. Figure 10 illustrates partition coefficients for selected elements and phases as a function of coexisting liquid composition.

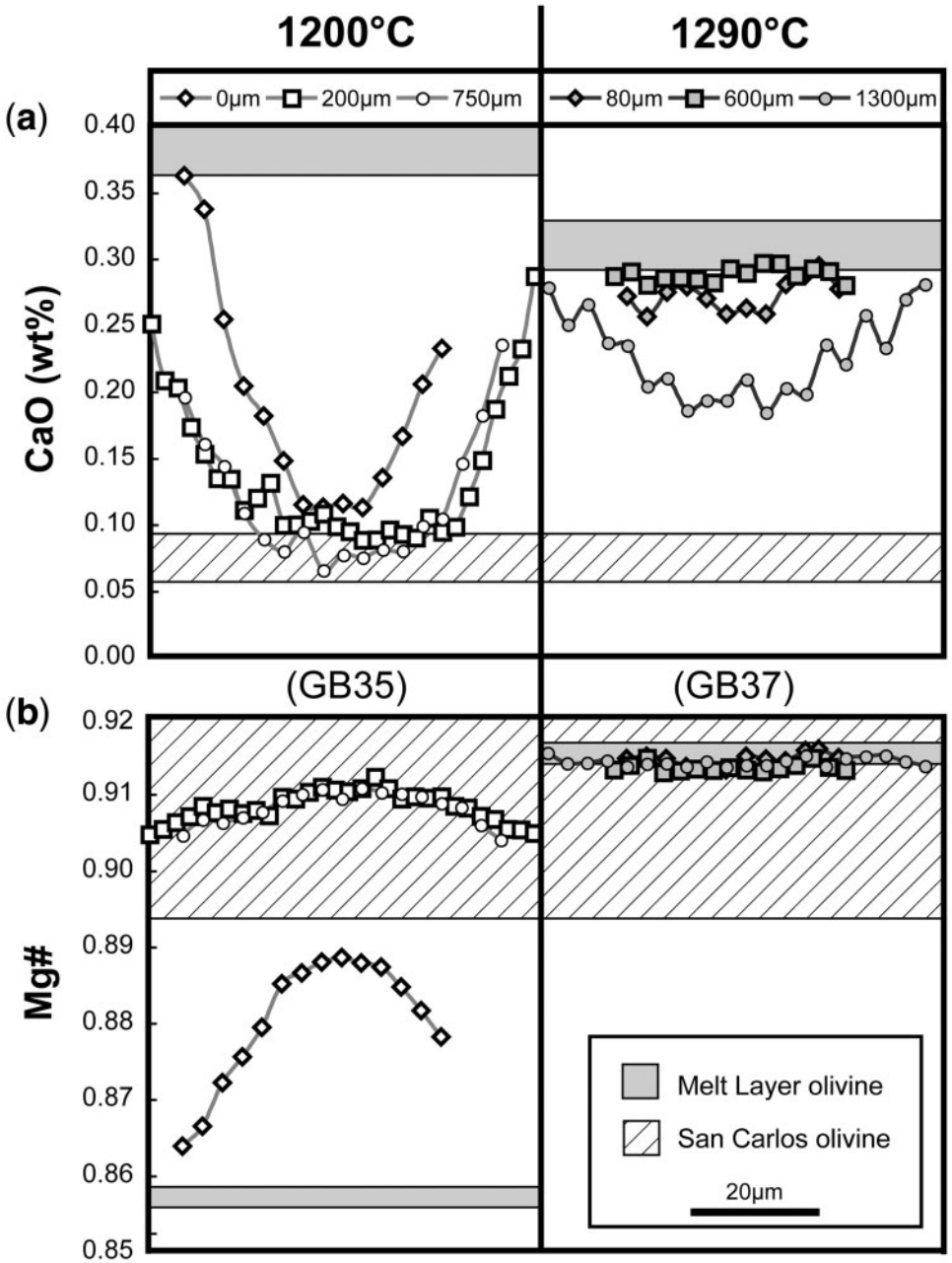

Fig. 5. Olivine rim-to-rim profiles as a function of distance to the present melt–peridotite interface (given in µm) for experiments at 1200°C (GB35) and 1290°C (GB37), compared with their respective ML olivine compositions. Also shown is the compositional range of San Carlos olivine used. (a) and (b) show CaO and Mg-number variability, respectively. In general, the level of equilibration increases towards the ML–PL interface and with higher run temperature. Equilibration with respect to Fe/Mg is faster than Ca equilibration, indicating diffusion rather than dissolution–reprecipitation processes at 1200°C and for the '1300 µm' grain at 1290°C. Also noteworthy is the asymmetry of the '0 µm' core in GB35 that is in direct contact with the ML at the more extensively equilibrated side.

Fe–Mg partitioning coefficients [$K_{D,Fe\text{-}Mg} = (FeO/MgO)^{phase}/(FeO/MgO)^{liquid}$] for olivine, opx and cpx in the ML are $0{\cdot}31 \pm 0{\cdot}04$, $0{\cdot}32 \pm 0{\cdot}06$ and $0{\cdot}32 \pm 0{\cdot}05$, respectively. Not included in these averages are data from the 1200°C runs, as the K_D calculations were compromised by extensive quench alteration of the glasses and MT liquids could not be used because of limited charge-scale equilibration at 1200°C (see Fig. 4). D_{Al} ($=Al_2O_3{}^{phase}/Al_2O_3{}^{liquid}$) values are $0{\cdot}32 \pm 0{\cdot}06$ for ML opx and $0{\cdot}32 \pm 0{\cdot}04$ for ML cpx. Ranges for ML cpx for D_{Na} ($=Na_2O^{phase}/Na_2O^{liquid}$), D_{Ti} ($=TiO_2{}^{phase}/TiO_2{}^{liquid}$), and D_{Ca} ($=CaO^{phase}/CaO^{liquid}$) are $0{\cdot}14 \pm 0{\cdot}02$,

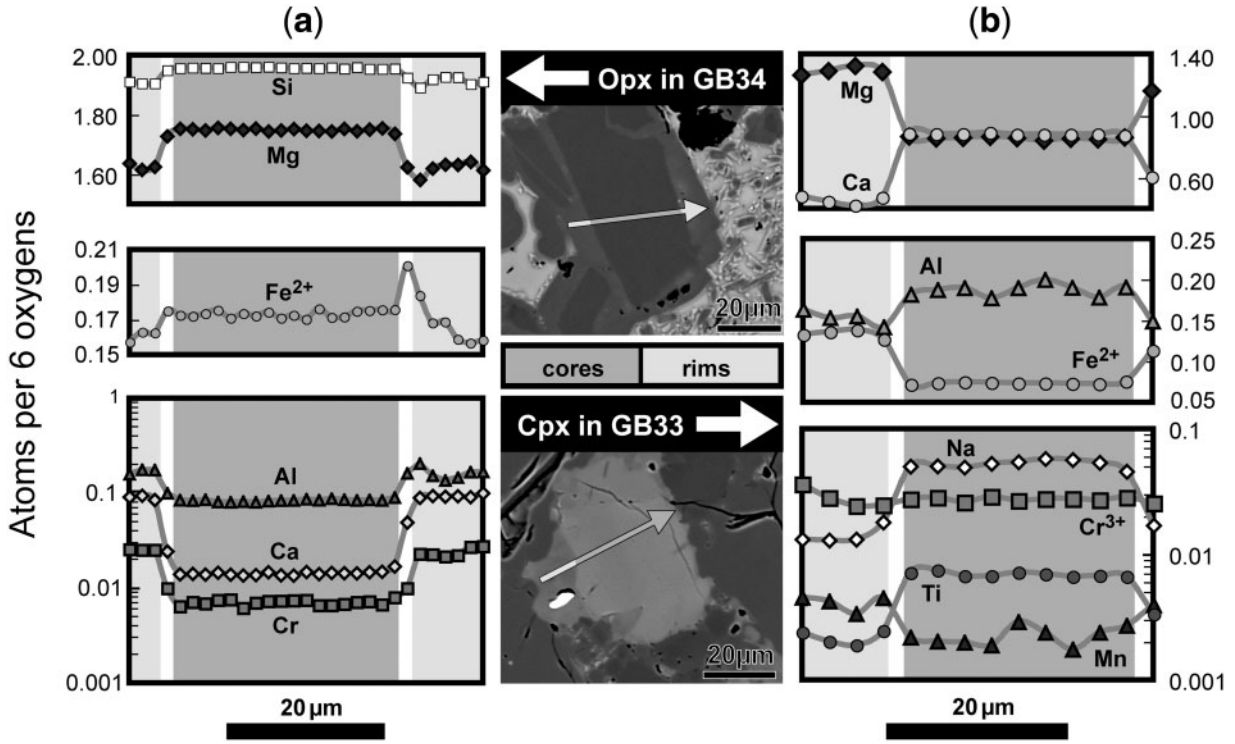

Fig. 6. Pyroxene rim-to-rim profiles reveal compositionally distinct cores and rims separated by sharp compositional discontinuities. (a) displays compositional trends across an opx grain at the ML–PL interface in run GB34 with a partially dissolved core and well-developed rims. (b) shows compositional trends across a cpx grain in GB33. In general, pyroxene core compositions are very constant and overlap with the original Balmuccia compositions. Rims show slight variations for some components, but heterogeneity overall remains small. The opx grain in (a) was selected for the substantial rim formed adjacent to the ML around a partially dissolved core. For opx grains deeper in the PL or in reaction with HK#19, the formed rims are usually thinner, permitting fewer good measurements.

$0{\cdot}38 \pm 0{\cdot}05$ and $1{\cdot}29 \pm 0{\cdot}12$, respectively. Distribution between ML plagioclase and liquid for $CaO/(Na_2O + K_2O)$ ranges from $1{\cdot}13 \pm 0{\cdot}03$ to $1{\cdot}93 \pm 0{\cdot}29$, with a mean value of $1{\cdot}46 \pm 0{\cdot}34$. This average is intermediate between the averages obtained by equilibrium crystallization experiments on HK#19.1 at 0·7 GPa ($1{\cdot}00 \pm 0{\cdot}09$) and 1·0 GPa ($1{\cdot}83 \pm 0{\cdot}04$) (Villiger *et al.*, 2004, 2007). All the other aforementioned partition coefficients for ML phases overlap also with values obtained in the crystallization experiments of Villiger *et al.* (2004, 2007). In the PL, partition coefficients for equilibrated rims and (re-)precipitates often display slightly more variation than observed for the equivalent ML mineral–liquid pairs. Nonetheless, the distribution coefficients for Fe–Mg (ol, opx and cpx vs liquid), Na and Ca (cpx vs liquid), and $CaO/(Na_2O + K_2O)$ (plag vs liquid) largely overlap at the 1σ level (see Table 5). However, PL D_{Al} values for opx ($0{\cdot}21 \pm 0{\cdot}07$) and cpx ($0{\cdot}25 \pm 0{\cdot}03$), and D_{Ti} values for cpx ($0{\cdot}30 \pm 0{\cdot}05$) are markedly lower than the equivalent ML pair values. This variable behavior will be discussed below.

Based on Na partitioning between cpx and liquid, calculated pressures based on the formula of Villiger *et al.* (2007) provide results consistent within the expected uncertainty for ML and equilibrium PL cpx (0·7–1·2 GPa; see Table 5).

DISCUSSION

Evaluation of the experimental strategy

The three-layer setup was intended to simulate melt flow at experimental length and time scales. In contrast to comparable studies (Daines & Kohlstedt, 1994; Lundstrom, 2003; Morgan & Liang, 2003, 2005) and for reasons described above, the run products were not annealed at super-solidus conditions. Instead, the layered setup was consolidated during a stage of hot isostatic pressing (the 'HIP stage') at sub-solidus conditions prior to the infiltration experimental stage.

The effectiveness of the HIP stage in consolidating the three-layer setup is demonstrated by the intact geometry after most experiments (e.g. run illustrated in Fig. 1). However, short-duration experiments (10–30 min at run temperature) revealed that the melt traps were filled entirely in the first few minutes after initiating the experiments. Because of this higher than expected melt-migration rate, there was only a short-lived period of

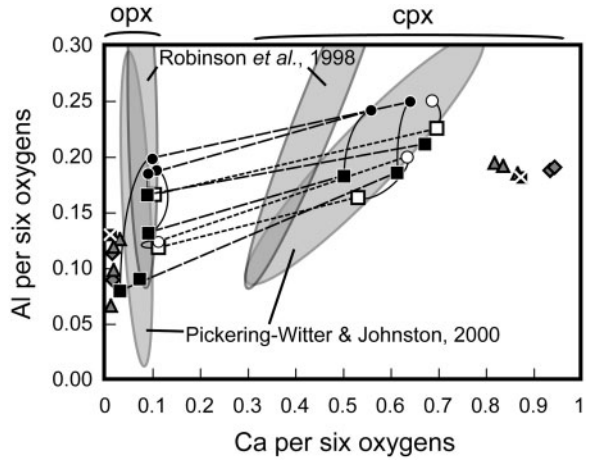

Fig. 7. Covariation of Al^{3+} and Ca^{2+} per six oxygens for opx and cpx, after Robinson *et al.* (1998) and Lo Cascio *et al.* (2004). Average Balmuccia pyroxenes (black squares with white cross) are plotted for comparison, revealing the occurrence of inherited cores with limited equilibration (grey symbols). Newly (re)precipitated pyroxenes are represented by squares for PL averages and circles for ML averages, and by open symbols for HK#19.v runs and black symbols for HK#20.v runs. Straight tie-lines connect coexisting opx and cpx. Pyroxenes from our experiments overlap with pyroxene compositions from melting experiments (Robinson *et al.*, 1998; Pickering-Witter & Johnston, 2000; shown as shaded fields), and pyroxenes in the harzburgite–clinopyroxenite reaction experiments of Lo Cascio *et al.* (2004), which plot in the same field as the Pickering-Witter & Johnston (2000) data. Curved tie-lines show that for a given run, commonly clear differences exist in ML vs 'rim' PL pyroxene compositions.

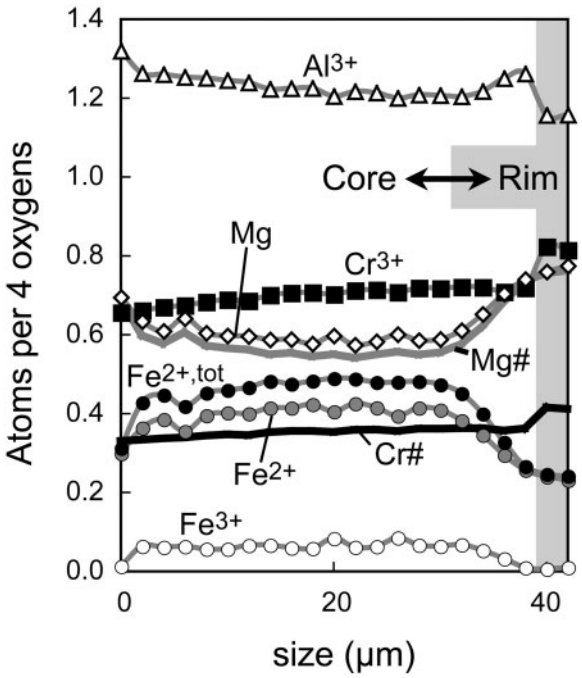

Fig. 8. Rim-to-rim compositional profiles of a spinel grain in run GB06 (same grain as shown in Fig. 2 at 1230°C) for several elements plotted as 'atoms per 4 oxygens', and Mg-number and Cr-number. The observed trends reveal a complex equilibration history, resulting from a combination of dissolution–reprecipitation and cation diffusion. (See text for a detailed discussion.)

advective melt flow, readily filling the initial porosity of the peridotite layer. As a result, the setup changed to a classic 'sandwich' setup, in which ML and PL are reaction couples that induce a chemical gradient over the experimental charge. The main difference with a classic 'sandwich' setup is the presence of infiltrated liquid in the peridotite layer at temperatures far below the peridotite solidus. The regime for crystal–melt equilibration changed accordingly to a situation where diffusion in the liquid phase could significantly contribute to equilibration between the melt and peridotite layers, also at peridotite sub-solidus conditions. This can be considered as equivalent to the natural case of reactive porous melt flow 'behind' an infiltration front. In consequence, although we did not achieve the simulation of reactive melt flow over the experimental run time, the experiments are viable for the evaluation of melt–peridotite reaction. A positive effect of the initial melt 'flush' is a quick reduction of porosity in both peridotite layer and melt trap, thereby reducing potential problems related to low-pressure melting.

The very low calculated Fe^{3+}/Fe_{tot} of spinel rims corroborates adjustment to the low fO_2 of the experimental setup employed (for thorough discussions, see Villiger *et al.*, 2004; Médard *et al.*, 2008).

Evaluation of the degree of equilibration

Compositional data obtained in this study often reveal large variations in phase compositions within a single experiment, both on charge-scale (Fig. 4) and grain-scale levels (Figs 5, 6 and 8). Although attainment of complete equilibrium was not our goal, this observation does raise questions about the relevance of the measured compositions and trends. On a grain-scale level, compositional variation is due to limited equilibration of initial BaSC phases (Table 4). In the discussion below, we concentrate on the question of whether the (intra- and extra-) charge-scale variations for rims and new precipitates indicate disequilibrium conditions or can be explained otherwise.

Evaluation of mineral–liquid equilibria

A first test for the validity of the phase compositions obtained in our experiments is based on solid phase–liquid element distribution. Although there is significant spread in 'new phase'–liquid partition coefficients from our experiments (see Table 5), this could potentially result from local equilibria, as opposed to being indicative of high levels of disequilibrium. As exemplified in numerous experimental studies (e.g. Hirschmann *et al.*, 1998; Lundstrom *et al.*, 1998; Draper & Green, 1999; Wasylenki

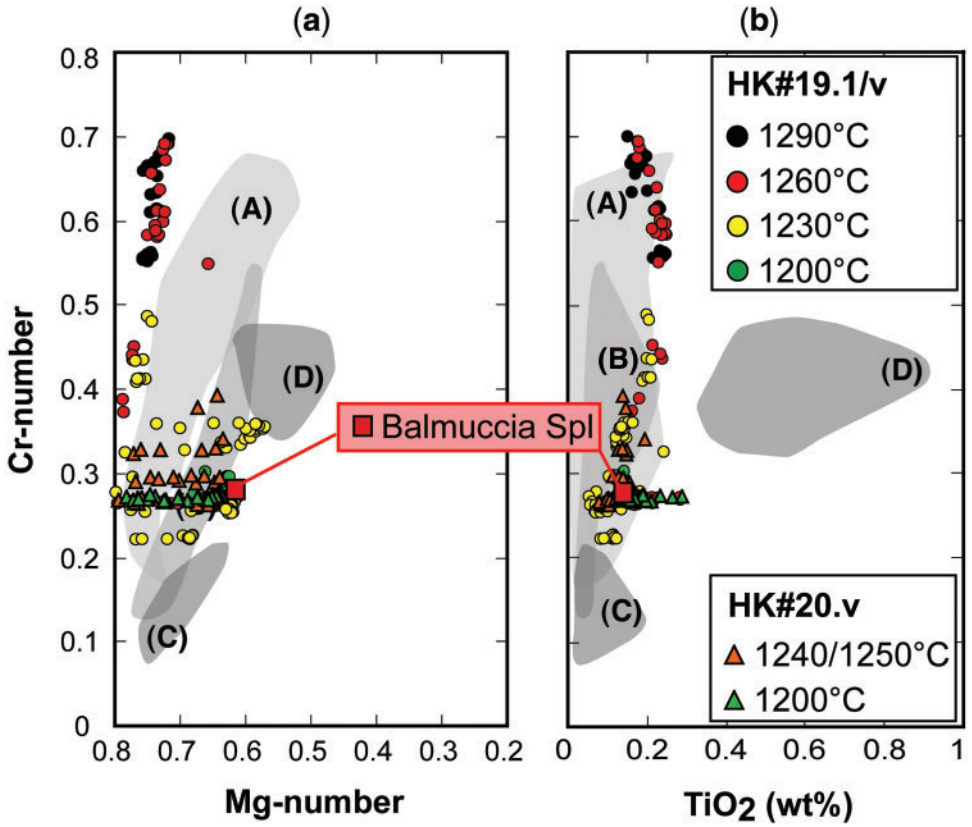

Fig. 9. Compilation of spinel compositions from this experimental study (data points) and comparison with natural spinel (shaded fields). (a) Cr-number vs Mg-number. (b) Cr-number vs TiO_2. Shaded fields are taken from Müntener & Manatschal (2006) and represent spinel from depleted harzburgite generated by high degrees of partial melting (A; Bernstein *et al.*, 1998), spinel from the Lena Trough recording deep melting and sodic metasomatism (B; Hellebrand & Snow, 2003), spinel from Alpine spinel- (C) and plagioclase- (D) peridotites (Müntener *et al.*, 2004; Müntener & Manatschal, 2006). Data from this study broadly plot on 'melting trends' observed in natural spinel, where higher Cr-number's represent higher degrees of partial melting.

et al., 2003; Gaetani, 2004; Johnston & Schwab, 2004; Villiger *et al.*, 2007), solid phase–liquid partitioning commonly depends—in addition to P and T—on melt and mineral compositions. For example, relatively small differences in the alkali contents of partial melts can have a significant impact on the activities of Si and Ca, especially at low melt fractions, and, therefore, on solid–liquid partitioning for these elements (e.g. Draper & Green, 1999; Hirschmann *et al.*, 1999; Wasylenki *et al.*, 2003).

Figure 10a reveals that Fe–Mg partition coefficients for ML and (rim-)PL data overlap, indicating a close approach to equilibrium on a charge-scale level. The same holds true for cpx–liquid values of D_{Na} (see Table 5) and, despite the notable spread in the data, of average ML and PL D_{Ca} ($1{\cdot}29 \pm 0{\cdot}12$ and $1{\cdot}28 \pm 0{\cdot}23$, respectively).

In contrast, D_{Al} and D_{Ti} for cpx–liquid (Fig. 10b) and D_{Al} for opx–liquid are significantly higher in the ML domains than for equivalent PL domains. For TiO_2, cpx–liquid distribution coefficients for MLs ($0{\cdot}38 \pm 0{\cdot}05$) fall within the range observed in crystallization experiments on HK#19.1 (Villiger *et al.*, 2007). The significantly lower PL values ($0{\cdot}30 \pm 0{\cdot}05$) in part overlap the $0{\cdot}22 \pm 0{\cdot}05$ range observed in a partial melting study on depleted peridotite DMM1 that is very similar in composition to BaSC (Wasylenki *et al.*, 2003). As a result of slow diffusion, Ti in cpx is thus mainly controlled by the liquid composition in the ML domain, and by the local mineralogy in the PL domain. This becomes even more apparent when the TiO_2/Al_2O_3 ratios of cpx and coexisting liquid (glass) are plotted against each other (Fig. 11). Increasing TiO_2/Al_2O_3 ratios as a result of decreasing T, or from PL to ML at any given T, result in increasing TiO_2/Al_2O_3 in coexisting cpx. Moreover, differences between ML and PL cpx–liquid partitioning become smaller at higher T as a result of more advanced equilibration over the experimental charge (see below). Our data plot at the lower end of a general, nearly linear positive correlation of TiO_2/Al_2O_3 in coexisting cpx and liquid, which reflects the dependence of pyroxene Ti solubility on the Al_2O_3 content of the liquid (see Villiger *et al.*, 2007, and references therein). However, the Al_2O_3 contents of the liquids do not change between MLs and their respective PLs in our experiments

Table 5: Solid phase–liquid partition coefficients for selected runs

		BaSC2 paired with:																												
		liquid composition HK#19.1												liquid composition HK#19.v									liquid composition HK#20.v								
		GB08			GB06			GB14			GB16			GB40			GB41			GB37			GB33			GB34			GB35		
		ML	R	C	ML	R	C	ML	R	C	ML	R	C	ML	R	C	ML	R	C	ML	R	C	ML	R	C	ML	R	C	ML	R	C
$K_{d,\ Fe\text{-}Mg}$																														
ol	Av	0·33		0·32	0·31	0·30	0·28	0·18*	0·17*	0·12*	0·28*	—	0·24*	0·32	0·32	—	0·35*	0·32*	0·30*	0·31	0·32	—	—	0·28	—	0·30	0·30	—	0·40	0·28	0·25
	SD	0·01		0·00	0·01	0·01	0·02	—	0·01	0·02	0·01	—	0·02	0·00	0·00	—	0·00	0·02	0·02	0·00	0·00	—	—	0·00	—	0·00	0·00	—	0·00	0·05	0·03
	n	19		7	11	8	37	1	10	15	9	—	25	15	12	—	12	8	47	6	64	—	—	35	—	19	52	—	5	12	49
cpx	Av	—	—	—	0·31	0·26	0·27	0·19*	0·12*	0·09*	0·30*	0·27*	0·20*	0·33	0·33	0·3	0·34*	0	0·27*	—	—	—	0·29	0·30	0·26	—	0·31	0·29	0·40	0·24	0·24
	SD	—	—	—	0·02	0·02	0·07	0·03	0·01	0·02	0·01	—	0·01	0·01	0·01	0·01	0·02	0·32*	0·02	—	—	—	0·01	0·01	0·03	—	0·00	0·03	0·04	0·02	0·12
	n	—	—	—	2	7	24	5	10	11	9	1	17	2	10	3	8	12	22	—	—	—	6	9	27	—	5	30	3	17	39
opx	Av	—	0·31	0·34	—	0·27	0·27	0·17*	0·11*	0·11*	0·32*	—	0·23*	—	0·31	0·32	—	0·29*	0·29*	—	0·31	0·34	0·27	0·28	0·28	0·29	0·31	0·30	0·38	—	0·25
	SD	—	0·01	0·01	—	0·01	0·01	0·01	0·00	0·00	0·01	—	0·01	—	0·01	0·01	—	0·00	0·00	—	0·01	0·01	0·01	—	0·01	0·01	0·03	0·01	0·01	—	0·02
	n	—	10	16	—	6	33	4	6	23	2	—	8	—	5	18	—	6	41	—	14	26	19	1	31	6	10	42	2	—	25
D_{Al}																														
cpx	Av	—	—	—	0·41	0·21	0·26	0·32	0·23	0·24	0·30	0·26	0·21	0·31	0·25	0·29	0·32	0·29	0·24	—	—	—	0·35	0·27	0·28	—	0·24	0·30	0·32	0·27	0·27
	SD	—	—	—	0·02	0·04	0·09	0·07	0·04	0·04	0·04	—	0·02	0·01	0·04	0·01	0·02	0·04	0·02	—	—	—	0·01	0·04	0·04	—	0·02	0·04	0·02	0·03	0·15
	n	—	—	—	2	7	24	5	10	11	9	1	17	2	10	3	8	12	22	—	—	—	6	9	27	—	5	30	3	17	39
opx	Av	—	0·12	0·20	—	0·12	0·12	0·24	0·15	0·16	0·34	—	0·12	—	0·19	0·14	—	0·22	0·15	—	0·16	0·21	0·28	0·25	0·19	0·29	0·26	0·16	0·26	—	0·10
	SD	—	0·01	0·02	—	0·04	0·06	0·05	0·02	0·03	0·00	—	0·06	—	0·03	0·04	—	0·03	0·04	—	0·04	0·03	0·01	—	0·01	0·02	0·03	0·02	0·02	—	0·03
	n	—	10	16	—	6	33	4	6	23	2	—	8	—	5	18	—	6	41	—	14	26	19	1	31	6	10	42	2	—	25
D_{Ti}																														
cpx	Av	—	—	—	0·37	0·25†	0·36†	0·43	0·31†	0·36†	0·44	0·36†	0·27†	0·34	0·29†	0·54†	0·36	0·38†	0·45†	—	—	—	0·33	0·24†	0·50†	—	0·25†	0·52†	0·41	0·32†	0·36†
	SD	—	—	—	0·04	0·05	0·14	0·16	0·07	0·04	0·06	NA	0·04	0·01	0·05	0·02	0·05	0·08	0·03	—	—	—	0·04	0·07	0·11	—	0·03	0·14	0·13	0·05	0·03
	n	—	—	—	2	7	24	5	10	11	9	—	17	2	10	3	8	12	22	—	—	—	6	9	0·27	—	5	30	3	17	39
D_{Na}																														
cpx	Av	—	—	—	0·14	0·22	0·37	0·17	0·18	0·45	0·12	0·12	0·24	0·17	0·15	0·35	0·12	0·13	0·28	—	—	—	0·15	0·15	0·53	—	0·14	0·38	0·13	0·13	0·32
	SD	—	—	—	0·01	0·04	0·12	0·05	0·03	0·15	0·02	—	0·07	0·00	0·02	0·02	0·01	0·02	0·06	—	—	—	0·02	0·01	0·14	—	0·03	0·16	0·01	0·02	0·13
	n	—	—	—	2	7	24	5	10	11	9	1	17	2	10	3	8	12	22	—	—	—	6	9	27	—	5	30	3	17	39
	$P^{\ddagger}_{\ddagger}$				1·0	1·4	2·0	1·1	1·2	2·3	0·7	0·7	1·5	1·2	1·0	2·0	0·8	0·8	1·7				1·0	1	2·4		0·9	2	0·8	0·8	1·8
D_{Ca}																														
cpx	Av	—	—	—	1·28	1·42	1·59	1·23	1·38	1·80	1·46	1·51	1·83	1·18	0·99	1·74	1·36	1·38	1·83	—	—	—	1·11	1·01	1·61	—	1·11	1·52	1·40	1·59	1·87
	SD	—	—	—	0·06	0·10	0·27	0·07	0·16	0·10	0·08	—	0·16	0·02	0·09	0·02	0·09	0·09	0·11	—	—	—	0·06	0·09	0·23	—	0·11	0·23	0·04	0·24	0·09
	n	—	—	—	2	7	24	5	10	11	9	1	17	2	10	3	8	12	22	—	—	—	6	9	27	—	5	30	3	17	39
$K_{d,\ Ca/(Na+K)}$																														
plg	Av	—	—	—	—	—	—	1·44	—	—	1·93	—	—	—	—	—	1·13	—	—	—	—	—	—	—	—	—	—	—	1·35	1·07	—
	SD	—	—	—	—	—	—	0·18	—	—	0·29	—	—	—	—	—	0·03	—	—	—	—	—	—	—	—	—	—	—	0·04	0·07	—
	n	—	—	—	—	—	—	2	—	—	6	—	—	—	—	—	12	—	—	—	—	—	—	—	—	—	—	—	4	2	—

*Calculated with MT glass composition to minimize problem with extensive ML quenching.
†Calculated with PL glass composition (see discussion).
‡Pressure (in GPa) calculated according to equation (2) of Villiger *et al.* (2007).
Av, average; SD, standard deviation; *n*, number of phase composition measurements; ML, melt layer; R, rim compositions; C, core compositions; —, phase not present.

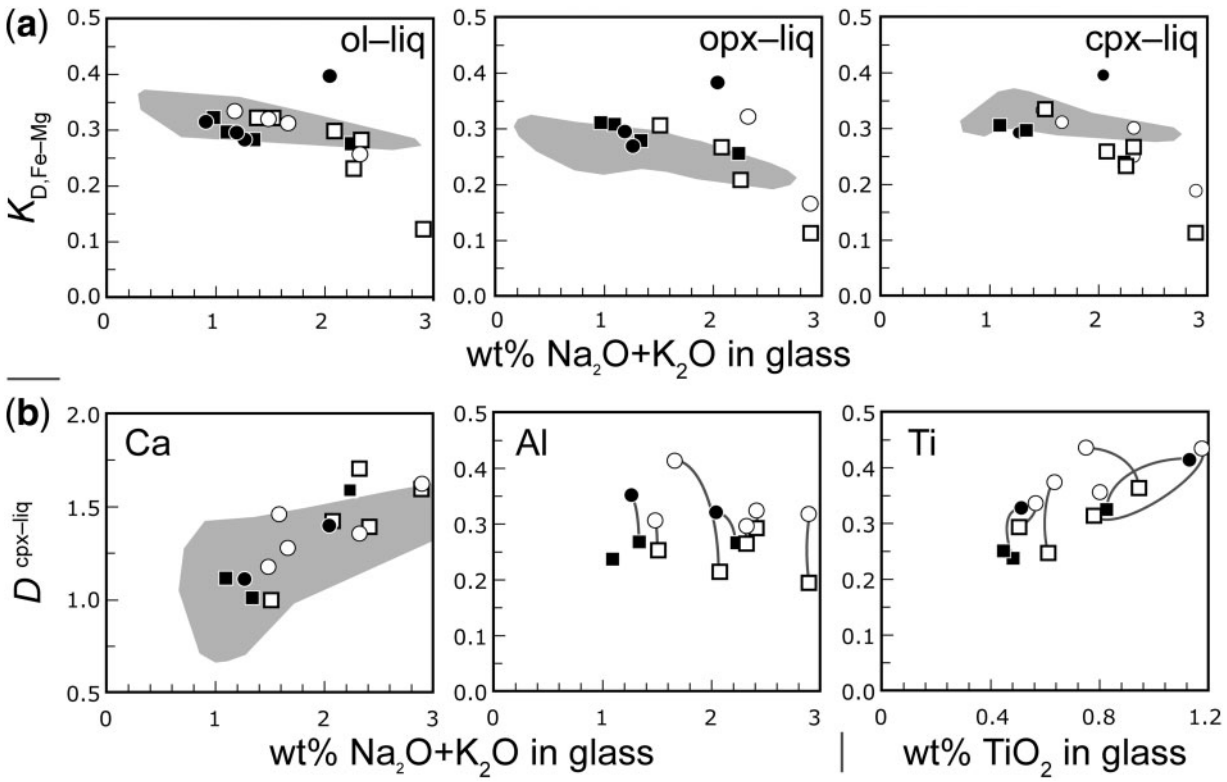

Fig. 10. (a) Fe–Mg partitioning of olivine, opx and cpx as a function of total alkali content (in wt %) of coexisting liquids. Open symbols represent runs with HK#19, whereas filled symbols correspond to runs using HK#20. Each circle represents the average of a ML of a particular run, and each square a PL average. Shaded fields represent K_D values obtained from a 10 kbar melting study on depleted peridotite (Wasylenki *et al.*, 2003). (b) Element partitioning between cpx and liquid for Ca, Al and Ti, as a function of coexisting liquid composition. Symbols are the same as in (a). The shaded field represents a compilation of D_{Ca} values reported in the literature for 0·9–1·2 GPa experiments (after Wasylenki *et al.*, 2003; data sources are listed in the caption of their fig. 5). Tie-lines connect MLs and PLs of single experiments for D_{Al} and D_{Ti}.

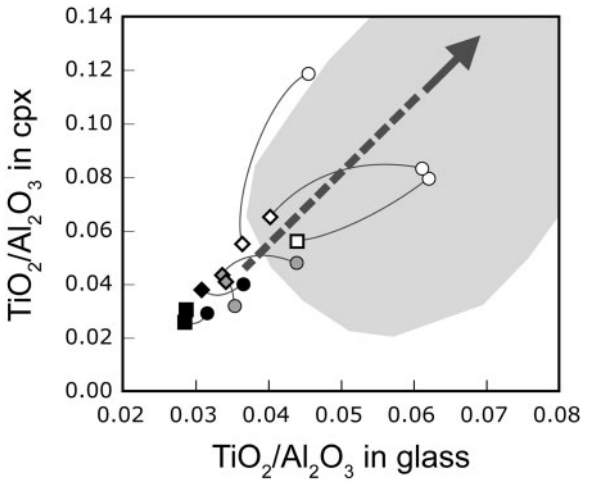

Fig. 11. TiO2/Al2O3 ratios of clinopyroxene as a function of the TiO2/Al2O3 ratio of the coexisting liquids (glass). Circles represent ML pairs, whereas diamonds and squares represent PL pairs from runs with HK#19 and HK#20, respectively. Black symbols relate to 1240–1260°C runs, gray symbols to 1230°C runs and white symbols to 1200°C runs. Tie-lines connect ML and PL data from single experiments. The shaded field represents data from anhydrous crystallization experiments that plot on a nearly linear positive trend as indicated by the arrow (see Villiger *et al.*, 2007, fig. 9b; data sources are listed in their fig. 6).

(Table 4). The systematic differences in TiO_2/Al_2O_3 between ML and PL cpx and liquid for any given run, thus, illustrate exclusively the control exerted by TiO_2 in coexisting liquids on Ti solubility in cpx.

Further comparison with experimental data from the literature provides additional constraints on meaningful 'in equilibrium' compositions for newly formed phases in this study. For example, the $K_{D,Fe-Mg}$ values for ol, opx and cpx in our study fall on the broad trends defined by literature data (Fig. 10a), showing a weak negative correlation with the alkali content of coexisting liquids. Moreover, cpx–liquid D_{Ca} values when plotted as a function of the alkali content of the coexisting liquid fall on the general positive trend observed in peridotite melting experiments (Fig. 10b) and overlap completely the DMM1 data (Wasylenki *et al.*, 2003). Therefore, although phase–liquid distribution coefficients can be a complex function of several factors, our calculated values (Table 5) for (re-)precipitated crystals and equilibrated rims overlap with those of the (appropriate) experimental 'equilibrium' data sets (e.g. Kinzler & Grove, 1992; Wasylenki *et al.*, 2003, and references therein; Villiger *et al.*, 2007).

Comparison with mineral compositions from the literature

Further evidence for the relevance of the phases formed in our experiments is obtained by comparison with phase compositions from the literature. Mg-numbers of newly formed olivine, opx and cpx all fall in the ranges expected for ultramafic upper-mantle lithologies. Exceptions are found in and close to the MLs in the 1200°C experiments, where the liquid is highly evolved and thus enriched in Fe, as expected from crystallization experiments (e.g. Villiger *et al.*, 2007). Moreover, Fig. 7 shows that for the newly formed pyroxenes from this study the Ca and Al contents and variations (broadly parallel tie-lines) are similar to those of equilibrium pyroxenes obtained in previous experimental studies (see Fig. 7 caption for data sources). Spinel displays a trend of increasing Cr-number with experimental run temperature that is also observed in natural samples, and is known to reflect varying amounts of partial melting (e.g. Dick & Bullen, 1984; Hellebrand *et al.*, 2001). The fairly high Mg-numbers (at Cr-number > ~0·4) relative to natural peridotite-hosted spinel reflect the fast quenching of our experiments, prohibiting subsolidus Fe–Mg re-equilibration with surrounding peridotite phases (see Kamenetsky *et al.*, 2001).

Partial equilibrium system

We can thus conclude from several lines of evidence that the newly formed phases and diffusively equilibrated rims surrounding inherited cores have compositions in equilibrium with upper-mantle peridotite and/or partial melts. As such, we can speak of a 'partial equilibrium system', in which the cores of the primary phases remain out of equilibrium, but the newly formed 'rims' and liquid are in equilibrium. Moreover, chromatographic effects occur in the infiltrating melt, thereby leading to extensive homogenization for fast diffusers (e.g. Na_2O, FeO and MgO), but distinct 'melt' and 'rock' signatures for slow diffusers (e.g. TiO_2, Al_2O_3). The influences of the resulting local equilibria on melt–rock reaction and compositions are considered further below.

Grain-scale reaction processes and local equilibria

None of the BaSC phases in the starting material are in equilibrium with the liquid at the run conditions employed. Consequently, interaction with the fractionated ML liquid leads to the textural, modal and compositional changes described above. In this section, we discuss the grain-scale processes and their relative importance for the various mineral phases. Generally, our observations correspond well to those described in a theoretical study by Liang (2003) and associated experimental studies (Morgan & Liang, 2003, 2005; Lo Cascio *et al.*, 2004). However, by using a fairly large grain size and compositions relevant for upper-mantle TBLs, we were able to provide improved insight into the kinetics of melt–rock equilibration in this domain of the mantle.

Olivine equilibration

Olivine records both diffusional equilibration between San Carlos cores and melt and dissolution ± (re-)precipitation. The 1200°C runs appear to display 'diffusional trends' for MgO and FeO m (Fig. 4); solid-state diffusion facilitated equilibration of olivine cores with local melt, and diffusion in the liquid facilitated equilibration between these local PL melts and the ML liquid. On the other hand, the flat profiles at 1290°C are the result of increased dissolution–reprecipitation. This shift in equilibration mechanism for olivine, from mainly diffusion at 1200°C to mainly recrystallization at 1290°C, is also reflected in olivine textures (Fig. 2) and rim-to-rim profiles (Fig. 5).

Olivine Mg–Fe interdiffusion modeling

A quantitative approach to investigate the equilibration mechanisms of olivine and melt is possible through diffusion modeling, involving Mg–Fe interdiffusion in olivine (Costa *et al.*, 2008). As a result of the irregular shape of the initial BaSC grains and the unknown orientation of the measured profiles with respect to the crystallographic axes, however, the modeling results presented here are at best semi-quantitative.

At 1200°C, diffusion profiles were fitted to one grain facing the melt layer (a grain from GB14 that is larger than the grain from GB35 depicted in Fig. 5b) and one grain from 750 μm deep in the PL of GB35 (see Fig. 5b). Mg–Fe diffusion trends for olivine grains facing the ML in the 1200°C runs GB14 and GB35 extend up to 40 μm inward. As the initial irregular BaSC2 grains are ~80 μm across, it is likely that even the innermost cores of these grains have been subject to diffusion from several directions. Moreover, the core of the 0 μm 1200°C grain is heterogeneous, which could be inherited, or a combined result of diffusive equilibration and an irregular initial shape. However, the Fe–Mg trend of the rim facing the ML is continuous and could be fitted with the diffusion model. Assuming a constant rim composition of $Fo_{85·3}$ and a system open to flux, the calculated duration of diffusive equilibration is ~600 h, or 40 times longer than the run time (Fig. 12a). The 1200°C grain 750 μm deep in the PL shows Fe–Mg fluctuations not only in the core, but also to the right-hand side of the profile (Fig. 12c). This irregular variation could again be inherited or result from an irregular grain shape, but it could also result from dissolution–reprecipitation, certainly towards the rim. The left-hand side, however, displays continuous Fe–Mg variation that could be fitted well by the diffusion model. Fixing the rim composition at $Fo_{90·4}$, the profile can be fitted for a time of ~60 h, or four times the run time (Fig. 12c). Alternatively, for the same timescale, the left side of the grain can be fitted when the boundary composition is not

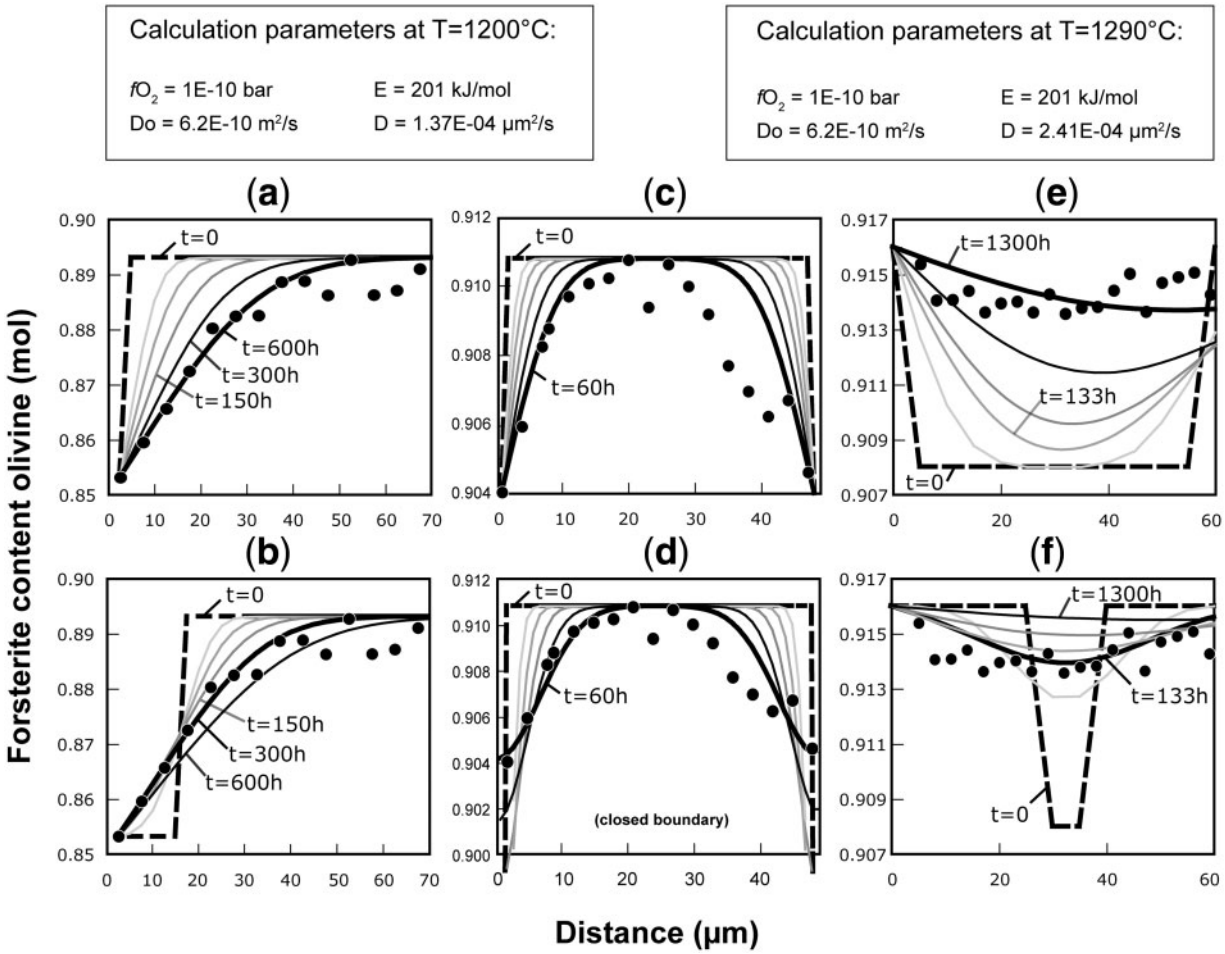

Fig. 12. Diffusion modeling of Fe–Mg variation in olivine with finite distances and compositionally dependent diffusion coefficients (see Appendix I of Costa *et al.*, 2008). Diffusion data are from Dohmen & Chakraborty (2007) and important calculation parameters are listed in the legends. The initial distribution ($t = 0$) of olivine compositions is depicted by a bold dashed line. A series of continuous lines shows for different times the inferred distribution, with continuous lines representing best fits to the data (filled circles). (a) and (b) display modeling of a grain in the 1200°C run GB14 that is adjacent to the ML. (a) shows fits to the data for diffusion alone, whereas (b) illustrates the case where a 17·5 µm thick rim of olivine was precipitated at $t = 0$, after which diffusion was allowed to take place. (c) and (d) display modeling of a grain in the PL, 1350 µm away from the ML, in the 1200°C run GB35. In (c) the boundary composition was fixed at the present rim composition, whereas in (d) a rim of 2 µm of olivine with 'ML composition' was introduced at both sides and the system was closed to flux. (e) and (f) illustrate modeling of a grain from the 1290°C run GB37. (e) shows fits to the data for diffusion alone, whereas (f) illustrates the case with a different initial distribution at $t = 0$. The latter represents an analogue for initial dissolution–reprecipitation and subsequent diffusive equilibration. (See text for a detailed discussion.)

fixed, but an initial 2 µm thick rim of $Fo_{85·7}$ is introduced and the system is closed to flux (Fig. 12d). The motivation for investigating this scenario is the short-lived initial stage of advective liquid flow from the ML into the MT that is inherent to our experimental setup. The initial melt flux provides melt in the PL that would precipitate 'ML olivine', thus with $Fo_{85·7}$ composition (see Table 4). The 2 µm 'rim' added at both sides as initial distribution therefore is an analogue of olivine precipitated from a small melt pocket, both continuously changing composition upon continuing reaction with the surrounding olivine.

The question arises as to why it is that the Fe–Mg profile of the grain from the interior of the PL can be fitted to four times the actual run time, whereas that of a grain adjacent to the ML can be fitted only to 44 times the actual run time. One explanation might be the presence of water in the starting liquid, as Fe–Mg interdiffusion can be up to 50 times faster under hydrous conditions as opposed to water-absent conditions (Hier-Majumder *et al.*, 2005). However, plagioclase crystallization, compositions and plagioclase–liquid $CaO/(Na_2O + K_2O)$ partitioning suggest nominally anhydrous conditions. Another explanation is precipitation of new olivine, combined with

diffusive equilibration of the old core and new rim. To model this scenario, initial growth of a 15 μm rim of 'ML olivine' ($Fo_{85·7}$) on the olivine core was assumed. As such, the Fe–Mg trend could be fitted after ~150–300 h, or 'only' 10–20 times the run time (Fig. 12b). Although still significantly longer than the actual run time, this result indicates that progressive growth of 'ML olivine', combined with continuous diffusive equilibration, could account for the thick 'diffusive' rims of olivine cores facing the ML.

Modeling of the 1290°C profiles depicted in Fig. 5b was more intractable, as ML olivine at 1290°C and the average San Carlos olivine compositions overlap ($Fo_{91·4 \pm 0·1}$ and $Fo_{90·8 \pm 0·7}$, respectively). Employing the average compositions for the largest grain depicted in Fig. 5b (the only one to display continuous CaO zoning) indicates that at least ~1300 h (87 times the run time) are needed to achieve an Fe–Mg profile that is reasonably flat and has a suitable composition (Fig. 12e). By assuming 22·5 μm dissolution–reprecipitation at each side, thereby retaining a core of 27·5 μm, we could achieve an acceptable result after ~222 h, or 32 times the run time. By retaining a core of only 7·5 μm, we could fit the profile already after ~133 h, or nine times the run time (Fig. 12f). This illustrates that dissolution–reprecipitation of olivine must play an important role in equilibration with the liquid at 1290°C.

Pyroxene equilibration

Opx and cpx show little to no diffusive equilibration with the melt (flat core profiles of Balmuccia compositions; e.g. Fig. 6), but both experience dissolution at all temperatures and reprecipitation if saturation is locally exceeded. This sometimes leads to 'mushroom' textures (see Darbellay *et al.*, 2008, for 'mushroom' garnet), where reprecipitated rims remain and cores are partially or completely dissolved.

Spinel equilibration

For spinel, textural and compositional observations also reveal a combination of dissolution–reprecipitation and diffusive equilibration at temperatures below 1260°C. At higher temperatures, dissolution without reprecipitation occurs.

In contact with a melt pocket, the partially dissolved (rounded) spinel grain depicted in Fig. 8 developed a reprecipitated rim with significantly increased Cr and decreased Al contents (higher Cr-number). Besides a diffusive trend of increasing Al that is limited in space to the rounded core, there is also a trend towards lower Fe (both Fe^{2+} and calculated Fe^{3+}) and higher Mg in the rims that extends continuously over the inherited core and the reprecipitated rim. This complex geometry with continuous zoning for some elements and discontinuous zoning for others over the core and rim can be explained as follows: (1) initial influx of HK#19.1 led to dissolution of the original spinel grain; (2) as saturation was locally reached, a rim reprecipitated in equilibrium with the melt at the run conditions, thus with higher Cr-number; (3) dissolution diminished or ceased temporarily as the core was protected by local saturation and formation of the newly formed rim. Subsequently, equilibration occurred predominantly through solid-state diffusion; for the fast diffusers Fe and Mg (and Al coupled with Fe^{3+}) this led to continuous zoning, whereas slow diffusers such as Cr and Al did not notably equilibrate between core and newly precipitated rim; (4) continuing equilibration with the ML liquid reservoir ultimately lowered the saturation in the local melt pocket to the extent that dissolution started again, as revealed by the small 'breaches' in the rim (bottom right of the grain) that extends into the inherited core.

Upon progressive melting of pyroxenes and spinel at higher run temperatures, melt fractions in PLs increase and diffusive communication with MLs becomes more effective. As a result, the PL melt pockets no longer reach saturation with respect to Balmuccia spinel, which will undergo dissolution without reprecipitation.

Significance of local equilibria

It is clear that whether or not a solid-solution phase undergoes dissolution–reprecipitation depends on whether or not local saturation is reached with respect to that phase. This is dependent on the composition of the local melt, which in turn is dependent on the starting composition, P–T conditions (fractionation of the ML, 'melting' of PL phases) and distance from the ML–PL interface. As suggested for peridotite melting (see Luth, 2002), the exact reaction mechanism upon melt infiltration may thus largely depend on a number of local factors (see below). This is also illustrated by the sensitivity to the small compositional change (most notably an increase in SiO_2 and a decrease in FeO; see Table 1) upon vitrification of HK#19.1 to form HK#19.v, which resulted in higher plagioclase stability (GB41 vs GB06) and lower spinel stability (no spinel formed in MLs of HK#19.v).

Influence of melt reactivity and grain size on formation of reactive boundary layers in experiments

Previous studies in comparison with ours

The experimental studies by Daines & Kohlstedt (1994) and Morgan & Liang (2003, 2005) were designed to investigate melt–peridotite reactions and formation of RBLs, with applications to melt flow regimes in the upper mantle. In these studies, fine-grained (≤10 μm) peridotite analogues and natural melt or synthetic analogues were pre-conditioned separately in synthesis runs at elevated T and P. As a consequence, the resultant peridotite analogues exhibited equilibrated textures with interstitial melt filling the porosity and reaction took place through

diffusive infiltration. It was shown that the reacting melt compositions, or more precisely their level of undersaturation with respect to a given peridotite phase, determine whether RBLs are formed in reaction with a mantle composition. More specifically, the rate of dunite growth in harzburgite and lherzolite dissolution runs was, to a good approximation, equal when the same initial melt composition was used (Morgan & Liang, 2003, 2005). However, the melt compositions used by Morgan & Liang are more reactive than typical partial melts expected to percolate through the TBL of adiabatically upwelling domains of the upper mantle. Moreover, the experiments of Daines & Kohlstedt (1994) were performed at rather low pressure (0·3 GPa). For these reasons, these studies are not directly applicable to melt flow (organization) in TBLs in the upper mantle.

The present study was performed with melt and peridotite compositions and at P–T conditions that are relevant for TBL domains at relatively slow spreading rates in the upper mantle above areas of partial melting. However, the PLs in our study remained texturally and compositionally rather poorly equilibrated after the 5 h HIP stage, with irregular grains of ~80 μm and about 6% of open porosity for BaSC2. Consequently, reaction was not only driven by diffusive infiltration of reactive melt, but was also facilitated by increased textural and compositional instability of initial grains and short-lived advective influx of reactive liquid. Despite these potential complications, distinct RBLs were formed in several runs.

Influence of infiltrating liquid on RBL formation

The influence of the infiltrating liquid composition on RBL formation was investigated by using two slightly different starting liquids. As illustrated in Fig. 13a and b, differences occur for the two slightly differing melt analogues HK#19 and HK#20. At 1290°C, both compositions are saturated in olivine only (Fig. 3a). As in all 15 h runs at 1290°C, cpx was dissolved in the entire PL in GB08, but additionally all opx was dissolved in a region ~100 μm thick adjacent to the HK#19.1 ML interface. Such a melt-bearing dunitic RBL was not developed in the equivalent run using HK#20 (GB37), as it is closer to opx saturation.

A similar dependence of RBL formation on the level of undersaturation of the reacting liquid was observed by Morgan & Liang (2005). By analogy with what is known from fluid–mineral dissolution (e.g. Lasaga & Luttge, 2001), the level of undersaturation in melt–rock reaction could control the mechanism, and therefore rate, by which crystal dissolution proceeds. At ~1260°C, HK#20 is saturated in ol and opx, whereas HK#19 is ol saturated but undersaturated with respect to both pyroxenes (Fig. 3a). For 15 h runs, opx volumes decreased to ~13–14 area % for reaction with both starting liquids. In the same experiments, cpx decreased to 4–5 area % upon reaction with HK#19 (GB05, GB40), whereas a vaguely defined cpx-free zone of ~380 μm developed upon reaction with HK#20 (GB34). The rest of the PL still contained ~1·5 area % cpx. At 1230°C and 1200°C, both HK#19 and HK#20 are very close to saturation or saturated in both opx and cpx, and as a result RBL formation could not be identified. However, as a result of the large grain size of BaSC2 with a high initial porosity and the sluggish reaction kinetics of pyroxenes (Morgan & Liang, 2005), BaSC2 is not ideally suited for the study of RBL formation. For example, we frequently observed increased amounts of reaction and thus higher amounts of interstitial melt adjacent to the ML, without formation of a lithologically definable RBL.

Influence of peridotite grain size on RBL formation

A smaller initial grain size would lead to a lower influence of dissolution kinetics, a more equal distribution of phases, and reduced advective flow, as the initial PL porosity would be smaller. To test this hypothesis, 15 h experiments were performed with the finer-grained BaSC3 peridotite mix and melt analogue HK#19.1 at run temperatures of 1290°C (GB23), 1260°C (GB24) and 1230°C (GB20).

At 1290°C, a pyroxene-free, melt-enriched dunite developed just as in the equivalent experiment GB08, but this time it was five times thicker (i.e. ~500 μm; Fig. 13c). At 1260°C and 1230°C, no visible RBLs were formed when using BaSC2. However, using the finer-grained BaSC3, a pyroxene-free dunitic RBL of ~80 μm thickness was formed at 1260°C, and an ~210 μm thick opx-free wehrlitic RBL was formed at 1230°C. Furthermore, the 1260°C run shows increased melt fractions for ~430 μm and reduced opx size for the first ~350 μm past the dunite–lherzolite interface. The 1230°C run also shows an ~350 μm wide zone of increased melt fraction (5·3 area % vs 1·8 area % deeper in the lherzolitic PL), without clear reduction in opx grain size. The total thicknesses of the melt-enriched PL domains (with respect to 'unreacted' lherzolite or, in the case of the 1290°C run, harzburgite) are approximately equal at all temperatures, i.e. ~500 μm at 1290°C and 1260°C and ~570 μm at 1230°C. It should be noted that these thicknesses are measured from the current ML–PL interface, which can differ from the initial interface through complete dissolution of the PL, especially at 1290°C.

In all three experiments significant amounts of melt were found in the melt trap. Therefore, the apparent 500–570 μm 'infiltration distance' of melt more probably represents a diffusive-infiltration or reaction front driven by limited diffusive equilibration with the ML. At 1290°C, this presumed diffusive infiltration front coincides with the lithological dunitic RBL, whereas the dunitic (1260°C) and wehrlitic (1230°C) RBLs trail the diffusive infiltration front as a result of sluggish pyroxene dissolution kinetics. With BaSC2, clear RBLs were not formed below 1290°C

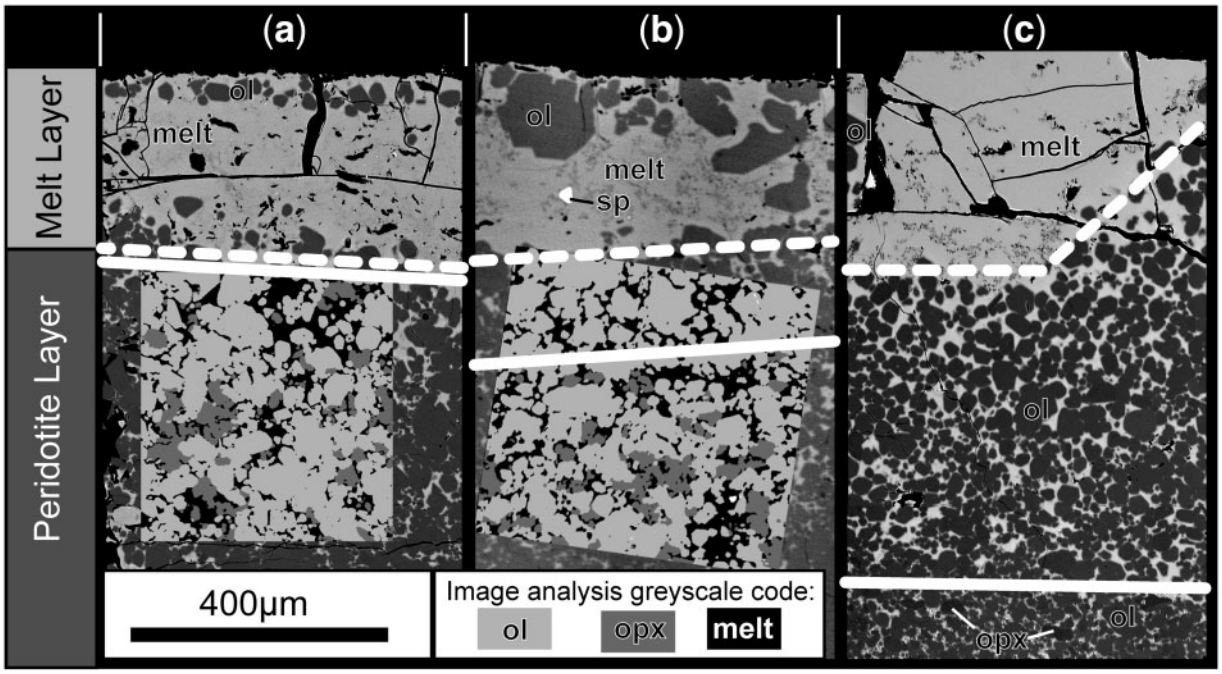

Fig. 13. A comparison of different 15 h, 1290°C runs, illustrating the influence of reacting liquid composition and initial grain size on RBL formation. (a) shows a run where BaSC2 was paired with HK#20 (GB37). (b) and (c) display runs that paired HK#19 with BaSC2 (GB08) and the finer-grained BaSC3 (GB23), respectively. In (a) and (b), the BSE images are overlain by maps that resulted from image analysis, to better show the distribution of the different minerals. Dashed white lines depict the current ML–PL interface, whereas continuous white lines indicate the border between harzburgite and the RBLs in which all opx was dissolved. Paired with HK#20, opx prevails in the PL up to the interface with the ML, whereas opx-free RBLs are formed in reaction with HK#19. (b) and (c) illustrate that for the same starting compositions, a smaller initial grain size results in a significantly better developed RBL.

because of these kinetic effects. However, detailed inspection of the 1230°C BaSC2 run GB06 shows a vaguely constrained area of 100–200 μm in which opx grains appear smaller than deeper in the PL, and the cpx mode is higher. Even with BaSC3, sluggish opx dissolution kinetics is demonstrated by opx grain size reduction over a large part of the diffusive infiltration zone at 1260°C.

The formation of a wehrlitic RBL at 1230°C, combined with occurrence of opx in the ML (a feature not observed in 15 h BaSC2-HK#19 experiments at 1230°C; see Fig. 3), reveals concurrency of several mass transfer processes. Destabilization of opx in favor of cpx (± ol ± melt) reveals lowered Si activity in the reactive infiltration area, probably as a result of diffusive infiltration of alkalis (see Lundstrom, 2003). Dissolution of opx will, amongst other compositional changes, lead to an important increase in SiO_2 in interstitial melt in the RBL. As the silica content of the ML liquid is lower than that in PL melt pockets, most silica will diffuse outwards towards the ML. There, opx will reprecipitate as soon as the Si activity is high enough. For BaSC2 experiments at 1230°C, this was achieved only in a 92 h experiment (GB09). The fact that opx precipitation in the ML occurs after only 15 h in BaSC3 experiment GB20 can be due to higher reactivity of the finer-grained BaSC3, and/or related to the smaller pores and hence lower permeability of the PL. The latter could lead to a more localized area of more intense reactive infiltration.

In summary, our experiments illustrate that kinetic effects have to be taken into account when studying reaction processes, particularly RBL formation, in experimental studies. Important non-intensive parameters are grain size, the related pore space and permeability. In the case of experimental studies, a smaller grain size will lead to sharper defined RBLs; this may or may not be a good approximation for natural systems.

Reactive boundary layer formation and melt transport in an upper-mantle TBL

When upper-mantle partial melts enter the TBL on their ascent through the uppermost mantle, a number of processes can occur; for example, fractional crystallization, diffusive equilibration through the melt and the solid, and dissolution ± reprecipitation of peridotite phases. As illustrated by our experiments, these processes can occur simultaneously and influence each other and are sensitive to local equilibria. By definition, P–T conditions in the TBL will lie around or slightly below the solidus of mantle peridotite. As follows from the present study, reaction between tholeiitic melt and depleted lherzolite may

lead to a significant increase in interstitial melt up to 30°C below the peridotite solidus temperature. Although dunitic RBLs were formed only at temperatures of 1260°C or higher, the incongruent preferential dissolution(–reprecipitation) of pyroxene(s) below this temperature will also increase permeability (e.g. Daines & Kohlstedt, 1994). Even though our starting peridotite mixture is not texturally equilibrated, this is a firm indication that melt percolation can remain or become focused in the TBL and that diffuse porous flow is also possible. However, as soon as the melt becomes saturated in one or more pyroxenes (or plagioclase at shallower depth), fractional crystallization may 'clog' the interconnected porosity of the dunitic melt channels or country rock. Therefore, melt flow over a significant distance in the TBL by means of diffuse or channelized flow is possible only when the flux of pyroxene (and/or plagioclase) undersaturated melt is high enough to prevent saturation. Oversaturation of a phase can be prevented by chemical shielding inside a dunitic channel (e.g. Kelemen *et al.*, 1995), as uptake of pyroxene components into the melt will be prevented. Alternatively, oversaturation may be prevented or delayed at high enough melt flux by the sluggish kinetics of pyroxene and formation of 'protective' rims by dissolution–reprecipitation (e.g. Klügel, 2001). Additionally, high influx of melt by channelized or pervasive porous flow may locally increase the temperature enough to reduce fractionation of phases from the melt (e.g. Müntener *et al.*, 2005). If oversaturation is not prevented by chemical and/or thermal 'shielding' and high fluxes, the melts will start to crystallize and progressively 'freeze' in the TBL. This process will refertilize the TBL peridotites both modally and chemically, as often described in abyssal and ophiolitic peridotites (e.g. Elthon, 1992; Dijkstra *et al.*, 2001; Müntener & Piccardo, 2003; Le Roux *et al.*, 2007).

Some previous experimental studies that investigated the formation of melt channels by reactive infiltration–dissolution (Daines & Kohlstedt, 1994; Morgan & Liang, 2003, 2005) have related the grain size of dunitic or harzburgitic RBLs to mantle permeability. The assumption made is that a larger grain size equals higher interconnected porosity and thus increased permeability (see McKenzie *et al.*, 1984). Indeed, Daines & Kohlstedt (1994) and Morgan & Liang (2003, 2005) observed the largest grain sizes and melt fractions in their experimental charges for dunitic RBLs. However, because they worked with fine-grained starting peridotite mixes that were annealed for (geologically) short times, we are of the opinion that too much weight was put on these grain-size observations. Textural ripening will go much faster upon reaction with a melt through dissolution–reprecipitation; thus the largest grain sizes would logically be found in RBLs when performing experiments with small PL grain sizes. Moreover, the fact that dunitic melt channels in the mantle sections of abyssal and ophiolitic peridotites usually display larger grain sizes could in part be due to subsolidus grain growth (see, e.g. Ohuchi & Nakamura, 2007).

We argue that melt flow regimes in the upper mantle, and in the TBL specifically, are controlled by the type and direction of reaction processes between melt and peridotite over a longer period of time. Incongruent dissolution of pyroxenes, with a consequent increase in melt fraction, will increase the connected porosity and thus permeability (Kelemen, 1990; Daines & Kohlstedt, 1994). Whether this effectively leads to channelized melt flow in high-porosity conduits by means of reactive infiltration instability (e.g. Aharonov *et al.*, 1995) may furthermore depend on small textural (e.g. Wark & Watson, 2000) and lithological (e.g. Liang & Guo, 2003) heterogeneities. Our observation that smaller grain sizes lead to increased rates of RBL formation is a further indication that channelization of melt flow can depend on mantle heterogeneity. Moreover, it has emerged from numerous case studies, for example on the Lanzo peridotite (see Müntener *et al.*, 2005, fig. 15) and abyssal peridotite from the Mid-Atlantic Ridge (see Suhr *et al.*, 2008, fig. 12), that melt flow regimes and consequently melt–rock reaction processes may change considerably during the geodynamic evolution of a mantle segment. As such, our experiments could be looked upon as representing 'snapshots' of the reaction processes, and by interpretation also of melt flow regimes, for their specific P–T and compositional conditions.

So far, we have only remotely introduced 'time' in our discussion of melt–rock reaction and melt flow organization in upper-mantle TBLs. As with any experimental high-P–T study, interpretations as a function of geological time-scales are complicated by limitations in sample size (equivalent to finite sizes of chemical reservoirs, thus limited chemical driving force for reaction), run times and physically driven melt flux. Consequently, quantitative extrapolation of our experimental results to the natural upper-mantle case is difficult. Although faced with the same complications, Morgan & Liang (2003, 2005) illustrated that the growth rates of RBLs in their experiments could be reproduced by fairly simple calculations, with SiO_2 diffusion in the melt as the rate-limiting factor. Using their formulae, they estimated replacive dunite growth rates for conditions prevalent beneath a mid-ocean ridge. One important conclusion from their order of magnitude calculations was that pure dissolution alone is unable to produce dunite channels wider than a few meters within time-scales of mantle upwelling under a mid-ocean ridge. As discussed above, our study demonstrates an important factor not taken into account by Morgan & Liang; that is, the influence of (sluggish) reaction of initial phases on RBL formation. For example, when running the same starting compositions at identical P–T–t conditions (0·8 GPa, 1290°C, 15 h), a dunitic RBL

of ~500 μm was formed within a BaSC3 PL, whereas it measured only ~100 μm when the coarser-grained BaSC2 peridotite mix was used (Fig. 13b and c, respectively). Therefore, the RBL formation rates derived by Morgan & Liang probably represent upper-limit values for reactive dissolution in the upper mantle. This reinforces their conclusion that dunite channel formation cannot result from diffusive infiltration alone. Consequently, we agree with their and previous researchers' findings (e.g. Kelemen, 1990; Asimow & Stolper, 1999; Braun & Kelemen, 2002) that large melt–rock ratios are necessary for the formation of upper-mantle dunitic melt conduits. Unfortunately, geologically relevant melt migration is one key parameter that is difficult to simulate in experimental studies, as proven by our attempt using the three-layer setup.

CONCLUSIONS

Our study has expanded the limited experimental data set on upper-mantle melt–rock reaction studies to melt and rock compositions and P–T conditions viable for TBLs overlying slowly upwelling asthenosphere. Using two slightly varying tholeiitic starting liquids and depleted peridotite mixtures with distinct grain sizes, over a temperature interval from just above to 60°C below the peridotite solidus, we come to the following main conclusions.

(1) At a grain-scale level, equilibration between reactive melt and mineral grains occurs by diffusion in the solid and/or dissolution–reprecipitation, or simply by dissolution. The exact equilibration mechanism depends on phase and liquid properties; that is, on the kinetics of diffusion and dissolution of a particular phase and on the level of undersaturation of the local melt with respect to that phase.

(2) On an experimental charge-scale level, reaction generally is most intense near the ML, leading locally to an increase in melt-filled porosity and sometimes to formation of lithologically definable RBLs. Dunitic RBLs are formed only at temperatures of at least 1260°C, but incongruent dissolution–reprecipitation of pyroxenes is significant until 30°C lower. The temperature dependence of RBL formation correlates directly to phase stability in the fractionating starting liquid. Our observation that RBL growth rates increase with decreasing grain size underlines that the sluggish kinetics of pyroxene dissolution is an important feature of upper-mantle melt–rock reaction.

(3) Compositions of newly formed phases and equilibrated rims of old cores mostly have compositions 'in equilibrium' with upper-mantle peridotite and/or partial melts. As a result of a combination of differences in diffusivities and consequently chromatographic effects in the melt, and the buffering capacity of the PL, compositional heterogeneity exists between new ML and PL phases. This is especially the case towards lower temperatures and for slow diffusers such as Ti and Al. Nonetheless, K_D calculations show that the new phases are in local equilibrium. Hence, our experiments represent partial equilibrium systems, with disequilibrium cores remaining and newly formed or well-equilibrated rims coexisting in equilibrium with local liquids.

Applied to melt migration in the TBL, these observations have some important implications. Assuming sufficient influx of 'fresh' melt, reactive porous flow is possible even at temperatures up to 30°C below the depleted peridotite solidus. To achieve channelized flow in dunitic channels, temperatures probably must be maintained at 1260°C at least, implying pervasive flow over longer timescales to counter the effect of conductive cooling. As illustrated by our experiments, dunite growth and hence channelization (through so-called 'reactive infiltration instability') could be promoted in regions of initially smaller grain sizes. In the case in which melt migration in the TBL, either channelized or diffuse, is 'slow' in relation to dissolution and melting kinetics, then the melts will become saturated readily in the surrounding peridotite phases by chemical equilibration and conductive heat loss. In upper-mantle TBL regions, this would lead inevitably to 'freezing' of the infiltrating melts, hence to refertilization of the TBL rocks. Thus, a general situation in TBLs is likely for infiltrating melts to first dissolve pyroxenes, spinel and/or plagioclase from the country rock ('depletion'), and higher in the column to partially or completely crystallize in the country rocks ('refertilization'). As such, refertilized rocks in (ultra-)slow-spreading systems and ophiolites trace a 'paleo-melt extraction' zone.

ACKNOWLEDGEMENTS

We would like to acknowledge F. Costa for providing a calculation sheet for diffusion modeling, and for helpful discussions. Moreover, we express our gratitude for thoughtful reviews by C. Herzberg, M. M. Hirschmann and an anonymous reviewer. This work was financially supported by the Swiss National Science Foundation (SNF Grant PP0022-102809). The Electron Microprobe Laboratory at the Institute of Geological Sciences at the University of Bern is supported by SNF Grant 200021-103479/1.

REFERENCES

Aharonov, E., Whitehead, J. A., Kelemen, P. B. & Spiegelman, M. (1995). Channeling instability of upwelling melt in the mantle. *Journal of Geophysical Research—Solid Earth* **100**, 20433–20450.

Asimow, P. D. & Stolper, E. M. (1999). Steady-state mantle–melt interactions in one dimension: I. Equilibrium transport and melt focusing. *Journal of Petrology* **40**, 475–494.

Beck, A. R., Morgan, Z. T., Liang, Y. & Hess, P. C. (2006). Dunite channels as viable pathways for mare basalt transport in the deep lunar mantle. *Geophysical Research Letters* **33**, L01202.

Berger, E. T. & Vannier, M. (1984). Les dunites en enclaves dans les basaltes alcalins des îles océaniques: approche pétrologique. *Bulletin de Minéralogie* **107**, 649–663.

Bernstein, S., Kelemen, P. B. & Brooks, K. (1998). Depleted spinel harzburgite xenoliths in Tertiary dykes from East Greenland: restites from high degree melting. *Earth and Planetary Science Letters* **154**, 221–235.

Boudier, F. & Nicolas, A. (1972). Fusion partielle gabbroïque dans la lherzolite de Lanzo (Alpes piémontaises). *Schweizerische Mineralogische und Petrographische Mitteilungen* **52**, 39–56.

Boyd, F. R. & England, J. L. (1960). Apparatus for phase-equilibrium measurements at pressures up to 50 kilobars and temperatures up to 1750°C. *Journal of Geophysical Research* **65**, 741–748.

Braun, M. G. & Kelemen, P. B. (2002). Dunite distribution in the Oman Ophiolite: Implications for melt flux through porous dunite conduits. *Geochemistry, Geophysics, Geosystems* **11**, 8603, doi:10.1029/2001GC000289.

Brey, G. P. & Köhler, T. (1990). Geothermobarometry in 4-phase lherzolites II: New thermobarometers, and practical assessment of existing thermobarometers. *Journal of Petrology* **31**, 1353–1378.

Costa, F., Dohmen, R. & Chakraborty, S. (2008). Time scales of magmatic processes from modeling the zoning patterns of crystals. In: Putirka, K. & Tepley, F. J. III, (eds) *Minerals, Inclusions and Volcanic Processes. Mineralogical Society of America, Reviews in Mineralogy and Geochemistry* **69**, 545–594.

Daines, M. J. & Kohlstedt, D. L. (1994). The transition from porous to channelized flow due to melt/rock reaction during melt migration. *Geophysical Research Letters* **21**, 145–148.

Darbellay, B., Robyr, M. & Baumgartner, L. (2008). *Geochimica et Cosmochimica Acta* **72**, A197.

Dick, H. J. B. & Bullen, T. (1984). Chromian spinel as a petrogenetic indicator in abyssal and alpine-type peridotites and spatially associated lavas. *Contributions to Mineralogy and Petrology* **86**, 54–76.

Dijkstra, A. H., Drury, M. R. & Vissers, R. L. M. (2001). Structural petrology of plagioclase peridotites in the west Othris mountains (Greece): Melt impregnation in mantle lithosphere. *Journal of Petrology* **42**, 5–24.

Dijkstra, A. H., Barth, M. G., Drury, M. R., Mason, P. R. D. & Vissers, R. L. M. (2003). Diffuse porous melt flow and melt–rock reaction in the mantle lithosphere at a slow-spreading ridge: A structural petrology and LA-ICP-MS study of the Othris Peridotite Massif (Greece). *Geochemistry, Geophysics, Geosystems* **4**, 8613, doi:10.1029/2001GC000278.

Dohmen, R. & Chakraborty, S. (2007). Fe–Mg diffusion in olivine II: point defect chemistry, change of diffusion mechanisms and a model for calculation of diffusion coefficients in natural olivine. *Physics and Chemistry of Minerals* **34**, 409–430.

Draper, D. S. & Green, T. H. (1999). *P–T* phase relations of silicic, alkaline, aluminous liquids: new results and applications to mantle melting and metasomatism. *Earth and Planetary Science Letters* **170**, 255–268.

Elthon, D. (1992). Chemical trends in abyssal peridotites—Refertilization of depleted suboceanic mantle. *Journal of Geophysical Research—Solid Earth* **97**, 9015–9025.

Falloon, T. J., Green, D. H., Danyushevsky, L. V. & Faul, U. H. (1999). Peridotite melting at 1·0 and 1·5 GPa: an experimental evaluation of techniques using diamond aggregates and mineral mixes for determination of near-solidus melts. *Journal of Petrology* **40**, 1343–1375.

Falloon, T. J., Green, D. H., Danyushevsky, L. V. & McNeill, A. W. (2008). Peridotite melting at 1·0 and 1·5 GPa: Implications for the petrogenesis of MORB. *Journal of Petrology* **49**, 591–613.

Gaetani, G. A. (2004). The influence of melt structure on trace element partitioning near the peridotite solidus. *Contributions to Mineralogy and Petrology* **147**, 511–527.

Hellebrand, E. & Snow, J. E. (2003). Deep melting and sodic metasomatism underneath the highly oblique-spreading Lena Trough (Arctic Ocean). *Earth and Planetary Science Letters* **216**, 283–299.

Hellebrand, E., Snow, J. E., Dick, H. J. B. & Hofmann, A. W. (2001). Coupled major and trace elements as indicators of the extent of melting in mid-ocean-ridge peridotites. *Nature* **410**, 677–681.

Hier-Majumder, S., Anderson, I. M. & Kohlstedt, D. L. (2005). Influence of protons on Fe–Mg interdiffusion in olivine. *Journal of Geophysical Research—Solid Earth* **110**, B02202, doi:10.1029/2004JB003292.

Hirose, K. & Kushiro, I. (1993). Partial melting of dry peridotites at high pressures: determination of compositions of melts segregated from peridotite using aggregates of diamond. *Earth and Planetary Science Letters* **114**, 477–489.

Hirschmann, M. M. (2000). Mantle solidus: Experimental constraints and the effects of peridotite composition. *Geochemistry, Geophysics, Geosystems* **1**, 2000GC000070.

Hirschmann, M. M., Baker, M. B. & Stolper, E. M. (1998). The effect of alkalis on the silica content of mantle-derived melts. *Geochimica et Cosmochimica Acta* **62**, 883–902.

Hirschmann, M. M., Ghiorso, M. S. & Stolper, E. M. (1999). Calculation of peridotite partial melting from thermodynamic models of minerals and melts. II. Isobaric variations in melts near the solidus and owing to variable source composition. *Journal of Petrology* **40**, 297–313.

Johnston, A. D. & Schwab, B. E. (2004). Constraints on clinopyroxene/melt partitioning of REE, Rb, Sr, Ti, Cr, Zr, and Nb during mantle melting: First insights from direct peridotite melting experiments at 1·0 GPa. *Geochimica et Cosmochimica Acta* **68**, 4949–4962.

Jurewicz, A. J. G. & Watson, E. B. (1988). Cations in olivine II. Diffusion in olivine xenocrysts, with applications to petrology and mineral physics. *Contributions to Mineralogy and Petrology* **99**, 186–201.

Kamenetsky, V. & Crawford, A. J. (1998). Melt–peridotite reaction recorded in the chemistry of spinel and melt inclusions in basalt from 43°N, Mid-Atlantic Ridge. *Earth and Planetary Science Letters* **164**, 345–352.

Kamenetsky, V. S., Crawford, A. J. & Meffre, S. (2001). Factors controlling chemistry of magmatic spinel: An empirical study of associated olivine, Cr-spinel and melt inclusions from primitive rocks. *Journal of Petrology* **42**, 655–671.

Kelemen, P. B. (1990). Reaction between ultramafic rock and fractionating basaltic magma I. Phase-relations, the origin of calc-alkaline magma series, and the formation of discordant dunite. *Journal of Petrology* **31**, 51–98.

Kelemen, P. B., Joyce, D. B., Webster, J. D. & Holloway, J. R. (1990). Reaction between ultramafic rock and fractionating basaltic magma II. Experimental investigation of reaction between olivine tholeiite and harzburgite at 1150°C–1050°C and 5 kB. *Journal of Petrology* **31**, 99–134.

Kelemen, P. B., Shimizu, N. & Salters, V. J. M. (1995). Extraction of mid-ocean-ridge basalt from the upwelling mantle by focused flow of melt in dunite channels. *Nature* **375**, 747–753.

Kelemen, P. B., Hirth, G., Shimizu, N., Spiegelman, M. & Dick, H. J. B. (1997). A review of melt migration processes in the adiabatically upwelling mantle beneath oceanic spreading ridges. *Philosophical Transactions of the Royal Society of London, Series A* **355**, 283–318.

Kinzler, R. J. & Grove, T. L. (1992). Primary magmas of midocean ridge basalts I. Experiments and methods. *Journal of Geophysical Research—Solid Earth* **97**, 6885–6906.

Klügel, A. (2001). Prolonged reactions between harzburgite xenoliths and silica-undersaturated melt: implications for dissolution and Fe–Mg interdiffusion rates of orthopyroxene. *Contributions to Mineralogy and Petrology* **141**, 1–14.

Köhler, T. P. & Brey, G. P. (1990). Calcium exchange between olivine and clinopyroxene calibrated as a geothermobarometer for natural peridotites from 2 to 60 KB with applications. *Geochimica et Cosmochimica Acta* **54**, 2375–2388.

Langmuir, C. H., Klein, E. M. & Plank, T. (1992). Petrological systematics of mid-ocean ridge basalts: constraints on melt generation beneath ocean ridges. In: Phipps Morgan, J., Blackman, D. K. & Sinton, J. M. (eds) *Mantle Flow and Melt Generation at Mid-Ocean Ridges. Geophysical Monograph, American Geophysical Union* **71**, 183–280.

Lasaga, A. C. & Luttge, A. (2001). Variation of crystal dissolution rate based on a dissolution stepwave model. *Science* **291**, 2400–2404.

le Roux, P. J., le Roex, A. P., Schilling, J. G., Shimizu, N., Perkins, W. W. & Pearce, N. J. G. (2002). Mantle heterogeneity beneath the southern Mid-Atlantic Ridge: trace element evidence for contamination of ambient asthenospheric mantle. *Earth and Planetary Science Letters* **203**, 479–498.

Le Roux, V., Bodinier, J. L., Tommasi, A., Alard, O., Dautria, J. M., Vauchez, A. & Riches, A. J. V. (2007). The Lherz spinel lherzolite: Refertilized rather than pristine mantle. *Earth and Planetary Science Letters* **259**, 599–612.

Liang, Y. (2003). Kinetics of crystal–melt reaction in partially molten silicates: 1. Grain scale processes. *Geochemistry, Geophysics, Geosystems* **4**, 1045, doi:10.1029/2002GC000375.

Liang, Y. & Guo, Y. (2003). Reactive dissolution instability driven by chemical diffusion with applications to harzburgite reactive dissolution. *Geophysical Research Letters* **30**, 1722.

Llovet, X. & Galan, G. (2003). Correction of secondary X-ray fluorescence near grain boundaries in electron microprobe analysis: Application to thermobarometry of spinel lherzolites. *American Mineralogist* **88**, 121–130.

Lo Cascio, M., Liang, Y. & Hess, P. C. (2004). Grain-scale processes during isothermal–isobaric melting of lherzolite. *Geophysical Research Letters* **31**, L16605.

Lundstrom, C. C. (2000). Rapid diffusive infiltration of sodium into partially molten peridotite. *Nature* **403**, 527–530.

Lundstrom, C. C. (2003). An experimental investigation of the diffusive infiltration of alkalis into partially molten peridotite: Implications for mantle melting processes. *Geochemistry, Geophysics, Geosystems* **4**, 8614.

Lundstrom, C. C., Shaw, H. F., Ryerson, F. J., Williams, Q. & Gill, J. (1998). Crystal chemical control of clinopyroxene–melt partitioning in the Di–Ab–An system: Implications for elemental fractionations in the depleted mantle. *Geochimica et Cosmochimica Acta* **62**, 2849–2862.

Luth, R. W. (2002). Possible implications of modal mineralogy for melting in mantle lherzolites. *Geochimica et Cosmochimica Acta* **66**, 2091–2098.

Lydon, J. W. (2005). The measurement of the modal mineralogy of rocks from SEM imagery: the use of Multispec© and ImageJ freeware. *Geological Survey of Canada, Open File* **4941**, 37 pp.

McKenzie, D. (1984). The generation and compaction of partially molten rock. *Journal of Petrology* **25**, 713–765.

Médard, E., McCammon, C. A., Barr, J. A. & Grove, T. L. (2008). Oxygen fugacity, temperature reproducibility, and H_2O contents of nominally anhydrous piston-cylinder experiments using graphite capsules. *American Mineralogist* **93**, 1838–1844.

Morgan, Z. & Liang, Y. (2003). An experimental and numerical study of the kinetics of harzburgite reactive dissolution with applications to dunite dike formation. *Earth and Planetary Science Letters* **214**, 59–74.

Morgan, Z. & Liang, Y. (2005). An experimental study of the kinetics of lherzolite reactive dissolution with applications to melt channel formation. *Contributions to Mineralogy and Petrology* **150**, 369–385.

Müntener, O. & Manatschal, G. (2006). High degrees of melt extraction recorded by spinel harzburgite of the Newfoundland margin: The role of inheritance and consequences for the evolution of the southern North Atlantic. *Earth and Planetary Science Letters* **252**, 437–452.

Müntener, O. & Piccardo, G. B. (2003). Melt migration in ophiolitic peridotites: the message from Alpine–Apennine peridotites and implications for embryonic ocean basins. In: Dilek, Y. & Robinson, P. T. (eds) *Ophiolites in Earth History. Geological Society, London, Special Publications* **218**, 69–89.

Müntener, O., Pettke, T., Desmurs, L., Meier, M. & Schaltegger, U. (2004). Refertilization of mantle peridotite in embryonic ocean basins: trace element and Nd isotopic evidence and implications for crust–mantle relationships. *Earth and Planetary Science Letters* **221**, 293–308.

Müntener, O., Piccardo, G. B., Polino, R. & Zanetti, A. (2005). Revisiting the Lanzo peridotite (NW-Italy): 'Asthenospherization' of ancient mantle lithosphere. *Ofioliti* **30**(2), 111–124.

Ohuchi, T. & Nakamura, M. (2007). Grain growth in the forsterite–diopside system. *Physics of the Earth and Planetary Interiors* **160**, 1–21.

Ortoleva, P., Chadam, J., Merino, E. & Sen, A. (1987). Geochemical self-organization. 2. The reactive-infiltration instability. *American Journal of Science* **287**, 1008–1040.

Pickering-Witter, J. & Johnston, A. D. (2000). The effects of variable bulk composition on the melting systematics of fertile peridotitic assemblages. *Contributions to Mineralogy and Petrology* **140**, 190–211.

Quick, J. E. (1981). The origin and significance of large, tabular dunite bodies in the Trinity Peridotite, Northern California. *Contributions to Mineralogy and Petrology* **78**, 413–422.

Rampone, E., Piccardo, G. B., Vannucci, R. & Bottazzi, P. (1997). Chemistry and origin of trapped melts in ophiolitic peridotites. *Geochimica et Cosmochimica Acta* **61**, 4557–4569.

Robinson, J. A. C., Wood, B. J. & Blundy, J. D. (1998). The beginning of melting of fertile and depleted peridotite at 1·5 GPa. *Earth and Planetary Science Letters* **155**, 97–111.

Schiano, P., Clocchiatti, R., Shimizu, N., Weis, D. & Mattielli, N. (1994). Cogenetic silica-rich and carbonate-rich melts trapped in mantle minerals in Kerguelen ultramafic xenoliths: Implications for metasomatism in the oceanic upper mantle. *Earth and Planetary Science Letters* **123**, 167–178.

Schiano, P., Provost, A., Clocchiatti, R. & Faure, F. (2006). Transcrystalline melt migration and Earth's mantle. *Science* **314**, 970–974.

Seyler, M. & Bonatti, E. (1997). Regional-scale melt–rock interaction in lherzolitic mantle in the Romanche Fracture Zone (Atlantic Ocean). *Earth and Planetary Science Letters* **146**, 273–287.

Seyler, M., Lorand, J. P., Toplis, M. J. & Godard, G. (2004). Asthenospheric metasomatism beneath the mid-ocean ridge: Evidence from depleted abyssal peridotites. *Geology* **32**, 301–304.

Shervais, J. W. (1979). Thermal emplacement model for the Alpine lherzolite massif at Balmuccia, Italy. *Journal of Petrology* **20**, 795–820.

Sobolev, A. V. & Shimizu, N. (1993). Ultra-depleted primary melt included in an olivine from the Mid-Atlantic Ridge. *Nature* **363**, 151–154.

Spiegelman, M., Kelemen, P. B. & Aharonov, E. (2001). Causes and consequences of flow organization during melt transport: The

reaction infiltration instability in compactible media. *Journal of Geophysical Research—Solid Earth* **106**, 2061–2077.

Stracke, A., Bourdon, B. & McKenzie, D. (2006). Melt extraction in the Earth's mantle: Constraints from U–Th–Pa–Ra studies in oceanic basalts. *Earth and Planetary Science Letters* **244**, 97–112.

Suhr, G., Hellebrand, E., Snow, J. E., Seck, H. A. & Hofmann, A. W. (2003). Significance of large, refractory dunite bodies in the upper mantle of the Bay of Islands Ophiolite. *Geochemistry, Geophysics, Geosystems* **4**(3), 8605, doi:10.1029/2001GC000277.

Suhr, G., Kelemen, P. & Paulick, H. (2008). Microstructures in Hole 1274A peridotites, ODP Leg 209, Mid-Atlantic Ridge: Tracking the fate of melts percolating in peridotite as the lithosphere is intercepted. *Geochemistry, Geophysics, Geosystems* **9**, 23.

Takahashi, N. (2001). Origin of plagioclase lherzolite from the Nikanbetsu peridotite complex, Hokkaido, northern Japan: Implications for incipient melt migration and segregation in the partially molten upper mantle. *Journal of Petrology* **42**, 39–54.

Ulmer, P. & Luth, R. W. (1991). The graphite–COH fluid equilibrium in P, T, fO_2 space—an experimental determination to 30 kbar and 1600°C. *Contributions to Mineralogy and Petrology* **106**, 265–272.

Van der Wal, D. & Bodinier, J. L. (1996). Origin of the recrystallisation front in the Ronda peridotite by km-scale pervasive porous melt flow. *Contributions to Mineralogy and Petrology* **122**, 387–405.

Villiger, S., Ulmer, P., Müntener, O. & Thompson, A. B. (2004). The liquid line of descent of anhydrous, mantle-derived, tholeiitic liquids by fractional and equilibrium crystallization—an experimental study at 1·0 GPa. *Journal of Petrology* **45**, 2369–2388.

Villiger, S., Ulmer, P. & Müntener, O. (2007). Equilibrium and fractional crystallization experiments at 0·7 GPa; the effect of pressure on phase relations and liquid compositions of tholeiitic magmas. *Journal of Petrology* **48**, 159–184.

Wark, D. A. & Watson, E. B. (2000). Effect of grain size on the distribution and transport of deep-seated fluids and melts. *Geophysical Research Letters* **27**, 2029–2032.

Wasylenki, L. E., Baker, M. B., Kent, A. J. R. & Stolper, E. M. (2003). Near-solidus melting of the shallow upper mantle: Partial melting experiments on depleted peridotite. *Journal of Petrology* **44**, 1163–1191.

White, R. S. (1988). The Earth's crust and lithosphere. *Journal of Petrology* **29**, 1–10.

Yaxley, G. M. (2000). Experimental study of the phase and melting relations of homogeneous basalt plus peridotite mixtures and implications for the petrogenesis of flood basalts. *Contributions to Mineralogy and Petrology* **139**, 326–338.

Zhang, H. F. (2005). Transformation of lithospheric mantle through peridotite–melt reaction: A case of Sino-Korean craton. *Earth and Planetary Science Letters* **237**, 768–780.